Mon. Not. R. Astron. Soc. **000**, 1–26 (2009) Printed 27 July 2010 (MN LATEX style file v2.2)

Gas sloshing, cold front formation, and metal redistribution: the Virgo cluster as a quantitative test case

E. Roediger[1⋆], M. Brüggen[1], A. Simionescu[2], H. Böhringer[3], E. Churazov[4,5] and W. R. Forman[6]

[1] *Jacobs University Bremen, PO Box 750 561, 28725 Bremen, Germany*
[2] *KIPAC, Stanford University, 452 Lomita Mall, Stanford, CA 94305, USA*
[3] *MPE, Gieenbachstr. 1, 85748 Garching, Germany*
[4] *MPA, Karl Schwarzschild Str. 1, 85748 Garching, Germany*
[5] *Space Research Institute (IKI), Profsoyuznaya 84/32, Moscow 117810, Russia*
[6] *Harvard-Smithsonian Center for Astrophysics, 60 Garden St., Cambridge, MA 02138, USA*

Accepted 1988 December 15. Received 1988 December 14; in original form 1988 October 11

ABSTRACT

We perform hydrodynamical simulations of minor-merger induced gas sloshing and the subsequent formation of cold fronts. Using the Virgo cluster as a test case, we show for the first time that the sloshing scenario can reproduce the radii and the contrasts in X-ray brightness, projected temperature, and metallicity across the observed cold fronts quantitatively.

We identify several new features typical for sloshing cold fronts: an alternating distribution of cool, metal enriched X-ray brightness excess regions and warm brightness deficit regions of reduced metallicity; a constant or radially decreasing temperature accompanied by a plateau in metallicity inside the cold fronts; a warm rim outside the CFs; and a large-scale brightness excess towards the responsible subcluster, which will be helpful for its identification. We can trace these new features not only in Virgo, but also in other clusters exhibiting sloshing cold fronts.

By comparing synthetic and real observations, we estimate that the causative minor merger event took place about 1 Gyr ago when a subcluster of 2–4 $\times 10^{13} M_{\odot}$ passed the Virgo core at 100 to 400 kpc distance, where a smaller mass corresponds to a smaller pericentre distance, and vice versa. Our line-of-sight is approximately perpendicular to the orbital plane of the subcluster. The most likely candidate is the galaxy group around NGC 4365, currently located about 5^o (1.6 Mpc) south of the Virgo centre.

Additionally, for the first time we quantify the metal redistribution by sloshing and discuss its importance.

We verify that the subcluster required to produce the observed cold fronts can be completely ram pressure stripped before reaching the Virgo centre, and discuss the conditions required for this to be achieved.

Finally, we demonstrate that the bow shock of a fast galaxy passing the Virgo cluster at ~ 400 kpc distance also causes sloshing and leads to very similar cold front structures. The responsible galaxy would be located about 2.2 Mpc north of the Virgo centre.

Key words: galaxies: clusters: individual: Virgo - galaxies: individual: M87 X-rays: galaxies: clusters methods: numerical

1 INTRODUCTION

During the last decade, high resolution X-ray observations have revealed a wealth of structure in the intra-cluster medium (ICM) of galaxy clusters, among them cold fronts. The first ones discovered were noticed as sharp discontinuities in X-ray brightness on one side of the cores of A2142 (Markevitch et al. 2000), A3667 (Vikhlinin et al. 2001), and the bullet cluster 1E 0657-56 (Markevitch et al. 2002). Temperature measurements revealed that these brightness edges

⋆ E-mail: e.roediger@jacobs-university.de

were not the expected bow shocks but cold fronts (CFs), where the brighter and denser side is also the cooler one. For a shock, the temperature jump across the brightness edge would be opposite. Several of such CFs associated with merging clusters have been found (see review by Markevitch & Vikhlinin 2007), hence they are called merger CFs. They have been interpreted as the contact discontinuity between the gaseous atmospheres of two different clusters.

Recent observations have detected a second class of CFs, named sloshing CFs after their most likely origin. Here, the CFs form arcs around the cool cores of apparently relaxed clusters. This type of CFs is the subject of this paper. For clarity, we will first introduce the sloshing scenario (Sect. 1.1) which is commonly believed to explain this type of CFs. Section 1.2 summarises the observational characteristics of sloshing CFs known so far. Targeting the CFs in the Virgo cluster, we show that the sloshing scenario can explain the observational characteristics not only qualitatively, but also quantitatively. Furthermore, we gather insights in the correct way of interpreting CF observations, and we uncover a number of new observational characteristics, which can also be transferred to other clusters. We will introduce the observation of the Virgo cluster in Sect. 1.3, explicate our aims in Sect. 1.4 and outline the structure of the paper in Sect. 1.5.

1.1 Gas sloshing scenario

Originally proposed by Markevitch et al. (2001) (see also review by Markevitch & Vikhlinin 2007), the idea of the sloshing scenario is the following: A gas-free subcluster falls through the main galaxy cluster, which initially has a near-hydrostatic ICM distribution. As the subcluster passes the main cluster's core, it slightly offsets the central gas in the main cluster core, but does not disrupt the main core. As soon as the subcluster has passed the central region and moves away, the offset ICM falls back towards the main cluster centre and starts to slosh inside the main potential well. Generally, the highest frequencies of sloshing occur at small radii. Thus, gas at a given radius moving into one direction will frequently encounter gas from larger radii still moving in the opposite direction. Such encountering flows lead to the formation of density, temperature, and consequently X-ray brightness discontinuities. The formation of a similar discontinuity occurs at the leading side of a cool cloud moving through a hotter ambient medium (Heinz et al. 2003). As the central cool gas moves outwards into regions of lower pressure, adiabatic expansion enhances the temperature contrast across the fronts. Thus, sloshing CFs are contact discontinuities between gas of different entropy, originating from different cluster radii. Usually, the subcluster passes the main cluster core at some distance, it transfers angular momentum to the ICM, and the sloshing happens in a spiral-like manner.

Ascasibar & Markevitch (2006) (AM06 hereafter) have performed hydrodynamical SPH+N-body simulations confirming this scenario. Clearly, the gravity of the subcluster does not only influence the main cluster's ICM, but also its DM distribution. However, the interaction with the subcluster induces only a slow motion of the central DM peak w.r.t. the overall cluster potential, while in the meantime the ICM sloshes inside the slowly moving central potential well. These simulations also demonstrated that the sloshing reproduces the morphology of observed CFs. In a small parameter study, the authors show that subclusters of different masses can produce sloshing and CF features, but less massive subclusters cause less clear signatures.

The authors also tested the impact of a subcluster containing a gaseous atmosphere of its own. They showed that the gas-gas interaction leaves clear observable signatures like a tail of ram-pressure stripped gas. As the clusters with observed sloshing CFs do not show such signatures, the scenario favours gas-free subclusters.

The simulations of ZuHone et al. (2010) are similar to the ones of AM06, but concentrate on the heating efficiency of the sloshing process.

As an alternative to the scenario described above, the oscillation of the central galaxy or central dark matter peak of the cluster has been proposed (Lufkin et al. 1995; Fabian et al. 2001; Tittley & Henriksen 2005). The moving central galaxy could experience ram pressure stripping by the surrounding ICM, and the contact discontinuity between the cooler central and warmer ambient gas could form the CFs. However, it is unclear whether this scenario would produce multiple fronts, which arise naturally in the sloshing scenario. Moreover, core oscillations should not leave traces a few 100 kpc outside the cluster core. We show that this should be the case for the sloshing scenario and link the observational detection of such large-scale features to cold fronts in the core.

Birnboim et al. (2010) propose that at least some CFs are caused by merging shocks. In this case, the CFs should form quasi-spherical rings around the cluster centre, and could be found at large radii out to 1 Mpc. We show that sloshing CFs are accompanied by a characteristic large-scale asymmetry, which would be absent in the shock-induced CFs.

1.2 Observed characteristics of sloshing CFs

Sloshing CFs manifest themselves as brightness edges forming arcs around the cool cores of clusters that otherwise appear relaxed and show no obvious signatures of recent merging (Markevitch & Vikhlinin 2007, Owers et al. 2009). Often, pairs or even triplets of edges appear on more or less opposite sides of the cluster core. Their morphology depends mainly on the angle between our line-of-sight (LOS) and the orbital plane of the subcluster: If the interaction is seen face-on, the edges form a spiral-like structure. If the LOS is parallel to the orbital plane, we see arcs on alternating sides of the cluster core. The brightness and temperature contrast across the edges is more modest compared to the merging CFs. Typical temperature contrasts range between 1.2 and 2.5.

This type of CFs is reported to be ubiquitous (Markevitch & Vikhlinin 2007, Ghizzardi et al. 2010), but high-resolution observations are available for only about 10 clusters: RX J1720.1+2638 (Mazzotta et al. 2001; Mazzotta & Giacintucci 2008; Owers 2008; Owers et al. 2009), MS1455.0+2232 (Mazzotta & Giacintucci (2008); Owers et al. (2009)), A2142 (Markevitch et al. 2000; Owers et al. 2009), A496 (Tanaka et al. 2006; Dupke et al. 2007), 2A0335+096 (Mazzotta et al. 2003; Sanders et al. 2009a), A2029 (Clarke et al. 2004; Million & Allen 2009), A2204

(Sanders et al. 2005, 2009b), Ophiuchus (Million et al. 2009), A1795 (Markevitch et al. 2001; Bourdin & Mazzotta 2008), Perseus (Churazov et al. 2003; Sanders et al. 2005), Centaurus (Fabian et al. 2005; Sanders & Fabian 2006). Our work will concentrate on the Virgo cluster, which is described in more detail in Sect. 1.3.

In addition to the edges in brightness and temperature, temperature maps show spiral- or arc-shaped cool regions inside the actual fronts. In X-ray brightness residual maps, an excess corresponding spatially to the structure in the temperature map is found (A2029, A2204, 2A0335+096, Perseus). For some clusters (RX J1720.1+2638, MS1455.0+2232, A496, Ophiuchus, 2A0335+096, A2204, Centaurus), even a corresponding structure in metallicity maps is seen. As X-ray brightness maps can be obtained more easily than temperature or metallicity maps, a spiral-shaped excess wrapped around the cluster core is often regarded as an indicator for ongoing sloshing.

Observations of medium depth do not allow the derivation of temperature and metallicity maps, but of radial profiles of these quantities across the CFs. For this purpose, the observational data is binned into circular/elliptical rings of a certain azimuthal length, resulting in an azimuthally averaged profile. At the CF, such profiles display a steep gradient at the radius of the CF.

1.3 The CFs in the Virgo cluster

Simionescu et al. (2010) (S10 hereafter) have presented XMM and Suzaku observations of a pair of CFs in the Virgo cluster: one CF is located about 90 kpc NW of the cluster centre, the other in the SE about 33 kpc from the cluster centre. In Fig. 1, we present two versions of residual X-ray brightness maps: The top panel shows the residual brightness w.r.t. the azimuthally averaged brightness. The bottom panel shows residuals w.r.t. the best-fitting radially symmetric beta model. This residual map is the same as Fig. 2 in S10, but in a colour scale used consistently throughout this paper.

Both residual maps show a sharp brightness edge in the NW. The edge in the SE is somewhat more subtle. The residuals w.r.t. the azimuthally averaged brightness clearly show a spiral-shaped excess in brightness, whereas there is only a trace of a spiral-shaped excess in the other version.

Simionescu et al. (2007) present a temperature and a metallicity map of the central 70 kpc of the Virgo cluster. Both show the southern cold front. The pointings outside 70 kpc are not deep enough to allow the derivation of a well-resolved temperature or metallicity map. Hence, S10 derive profiles of X-ray brightness, projected temperature, and metallicity across both CFs. For deriving these profiles, these quantities have been averaged over elliptical rings of 90^o azimuthal length. All three quantities show a steep gradient at the radius of the CF.

S10 already pointed out an asymmetry in the metallicity profiles between the NW and the SE direction. This indicates that, in addition to creating metallicity edges, sloshing also redistributes the heavy elements inside the cluster centre. S10 estimate that just inside the CFs, the metal density differs by about 20 to 30% between opposite sides.

We will extend the list of characteristics in Sect. 4.

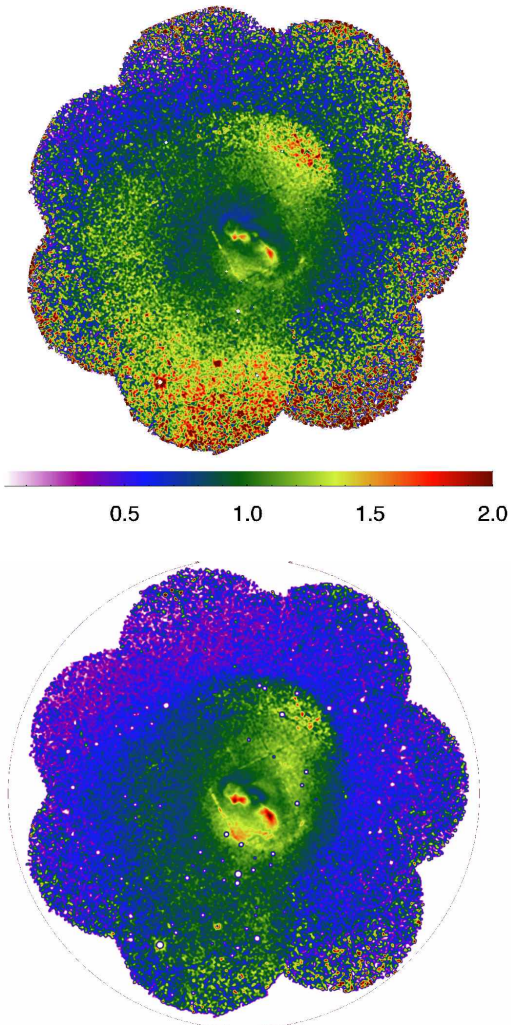

Figure 1. Observed residual maps (data/model) of the Virgo cluster. The top panel shows residuals w.r.t. the azimuthally averaged brightness. The bottom panel shows residuals w.r.t. a double-β profile fit to the observed X-ray brightness (same as in Simionescu et al. 2010, but with colour scale consistent to this paper).

1.4 Aims

Previous work has shown that the sloshing scenario (Sect. 1.1) can in principle explain the known observed characteristics (Sect. 1.2) of the resulting CFs. The quantitative characteristics of the CFs in Virgo (radius, contrast of X-ray brightness, temperature, metallicity across the edges, morphology in maps) depend on several parameters:

- characteristics of subcluster: mass, size, pericentre of orbit, velocity along orbit
- age: time since pericentre passage
- our line-of-sight (LOS) w.r.t. the orbit and orbital plane of the subcluster.

Our aims are as follows:

- Test the sloshing scenario quantitatively. We show that we can find a reasonable set of parameters to reproduce the observations well. Thus, we can constrain the merger history

of the Virgo cluster. We note that there is a degeneracy between subcluster mass and pericentre distance/velocity along orbit, so that only a combination of these can be constrained.

- Refine our understanding of observable signatures of sloshing CFs.
- Study the ability of sloshing to redistribute metals throughout the cluster core.
- Test if the basic ingredient of the scenario, i.e., that the subcluster is gas-free (see Sect. 1.1), can be true. Once we have identified a suitable subcluster, we show that a gaseous atmosphere could be ram-pressure stripped off this subcluster before it reaches the cluster core. However, the outcome of this test is not unique, and depends on the compactness of the subcluster's atmosphere.
- Test an alternative scenario: Churazov et al. (2003) propose that the passage of a shock through a cluster can cause the formation of CFs and demonstrated this with an idealised plane shock. We study the more realistic situation of the bow shock of a galaxy and its ability to trigger sloshing and CF formation.

To this end, we run hydrodynamical simulations of an idealised minor merger of a (gas-free) subcluster with a main cluster, which induces sloshing of the ICM of the main cluster. We perform a parameter study, varying the discussed parameters, specifically for the Virgo cluster, and perform a detailed comparison to the observations.

1.5 Outline of the paper

- Sect. 2 introduces our method.
- Sect. 3 describes our fiducial run.
- Sect. 4 is the core of this paper: it compares observations and simulation results in great detail. We show that the sloshing scenario can reproduce the currently known CF features. Moreover, we uncover some new characteristics, which are found in observations and simulations.
- Sect. 5 analyses the metal transport due to sloshing.
- Sect. 6 tests influence of a gas containing subcluster.
- Sect. 7 describes sloshing triggered by the bow shock of a passing galaxy.
- Sect. 8 discusses our results.
- Sect. 9 summarises.

2 METHOD

We run a set of idealised merger simulations, modelling the interaction between a massive galaxy cluster ("main cluster") and a smaller subcluster ("disturber"). We concentrate on minor mergers, where the disturber is significantly less massive than the main cluster. A major merger would cause additional structure, e.g., destroy the cool core, which is not the case for sloshing CF clusters. AM06 have shown that the formation of CFs is due to sloshing of the central ICM of the main cluster in the slowly moving DM peak of the main cluster, and that the gas sloshing proceeds on a much shorter time scale than the motion/oscillation of the DM core. Virgo contains only two CFs, which arise before the disturber passes the main cluster centre a second time (shown lateron). Hence, we will only model the first core passage of the subcluster and the subsequent gas sloshing. These restrictions allow us to neglect the evolution of the DM distribution of both clusters. We will use static potentials for both, the disturber and the main cluster. Given that the Jeans length is typically larger than 1 Mpc, we neglect the self-gravity of gas. These simplifications reduce computational costs significantly, which in turn allows us to run our simulations with high resolution and perform a detailed parameter study. In using static potentials for the main and the subcluster, we ignore that both, the subcluster's DM halo and the central DM distribution of the main cluster will suffer tidal truncation to some degree. However, tidal truncation does not happen instantaneously. For the sloshing scenario, the essential impact of the subcluster happens around pericentre passage. A subsequent mass loss due to tidal truncation should not modify our results significantly. Nonetheless, we regard the results of our simulations as upper limits on the strength of the effect on the ICM.

In the Virgo cluster, in most parts but the inner few kpc, i.e. in all our regions of interest, the cooling time is longer than 2 Gyr. Therefore we neglect radiative cooling in our simulations.

2.1 Code

Our simulations are run using the FLASH code (version 3.2., Dubey et al. 2009). FLASH is a modular block-structured AMR code, parallelized using the Message Passing Interface (MPI) library. It solves the Riemann problem on a Cartesian grid using the Piecewise-Parabolic Method (PPM). The simulations are performed in 3D and all boundaries are reflecting. We use a simulation grid of size $3 \times 3.5 \times 3\,\mathrm{Mpc}^3$. Due to Virgo's very steep central potential, we resolve the innermost 8 kpc with $\Delta x = 0.25\,\mathrm{kpc}$, using 8 levels of refinement. We resolve the inner 60 kpc with 1 kpc, and the inner 150 kpc with 2 kpc, and enforce decreasing resolution with increasing radius from the cluster centre to optimise computational costs. However, the position of the subcluster is always resolved to at least 2 kpc.

2.2 Tracing metallicity

In order to follow the evolution of metal distribution of the ICM, we utilise a mass scalar provided by the FLASH code, which acts as a tracer fluid. We start from a given metal density profile and follow its modification by the gas sloshing. As we want to concentrate on the redistribution of the metals, we do not inject metals during the simulation.

2.3 Model setup

The Virgo cluster ICM is modelled by a spherically symmetric density and temperature profile, chosen to fit observational data. These two quantities together fix the pressure profile and thus the pressure gradient. By assuming the gas to be in hydrostatic equilibrium, we calculate the gravitational acceleration due to the underlying cluster potential as a function of radius and thus the underlying cluster potential and mass profile. (See Sect. 2.4.1.) If the cluster is allowed to evolve for 2 Gyr without the subcluster passing, no sloshing or other modification of the ICM distribution is

Table 1. Attribution of grid directions to directions in the sky.

LOS	$-x$	$+x$	$-y$	$+y$	$-z$	$+z$
z	E	W	S	N	-	-
x	-	-	S	N	E	W

observed, meaning the initial setup is indeed in hydrostatic equilibrium.

Once we know the main cluster's potential, we calculate the orbit of a test mass moving through this potential.

Finally, we add the potential/gravitational acceleration of the subcluster. Initially, the subcluster is placed at a distance of approximately 0.5 Mpc from the cluster centre and given an appropriate initial velocity (see Sect. 2.4.3). Appendix B shows that the choice of initial separation influences our results only weakly. During the course of the simulation, the subcluster potential is shifted through the main cluster following the orbit derived above. The orbits are shown in Fig. 3. The initial time is chosen such that pericentre passage happens at $t = 0$.

We stop the simulations at $t = 1.2\,\mathrm{Gyr}$ after core passage ($t = 0$), when a good match to the observed CFs in Virgo is reached. This moment is well before the second core passage of the subcluster, and thus well within the restrictions of the rigid potential approximation.

We identify the directions in our simulation grid with the directions in the sky as given in Table 1, i.e. our maps will be oriented as usual: north (N) is up and east (E) is left.

2.4 Cluster models

2.4.1 Main cluster

Figure 2 summarises the characteristics of our Virgo cluster model. The first panel shows observational data for the electron density, n_e, from the ACCEPT sample (Cavagnolo et al. 2009) and the deprojected profile from Forman et al. (in prep.), along with a single-beta fit from Churazov et al. (2008), and a double-beta fit from Matsushita et al. (2002). In order to model the Virgo cluster as accurately as possible, we fit the deprojected data with a double-β model, which is shown by the black line. The second panel shows the observed projected temperature profile from the ACCEPT sample, the deprojected data from Forman et al., and a fit from Churazov et al. (2008). We fit the deprojected data with

$$\begin{aligned} T(r) &= T_1(r)C(r) + T_2(r)[1 - C(r)], \text{where} \qquad (1)\\ T_1(r) &= m_1 \cdot r + T_{01},\\ T_2(r) &= m_2 \cdot r + T_{02},\\ n_2 &= (m_1 - m_2)r_{\mathrm{break}} + n_1 \Leftrightarrow T_1(r_{\mathrm{break}}) = T_2(r_{\mathrm{break}}),\\ C(r) &= 1 - \frac{1}{1 + \exp\left(-\frac{r - r_{\mathrm{break}}}{a_{\mathrm{break}}}\right)}, \end{aligned}$$

which connects two linear functions smoothly. At large radii, we use a constant temperature, contrary to the fit of Churazov et al. (2008). The next panel shows the pressure profiles resulting from the ACCEPT data, the Forman et al. data, the Churazov et al. (2008) fits, and our fits to density and temperature. Assuming hydrostatic equilibrium, we can calculate the underlying potential and the associated cumulative DM mass, which is shown in the fourth panel, along with the cumulative mass for the ICM atmosphere. Table 2 summarises our ICM fit parameters.

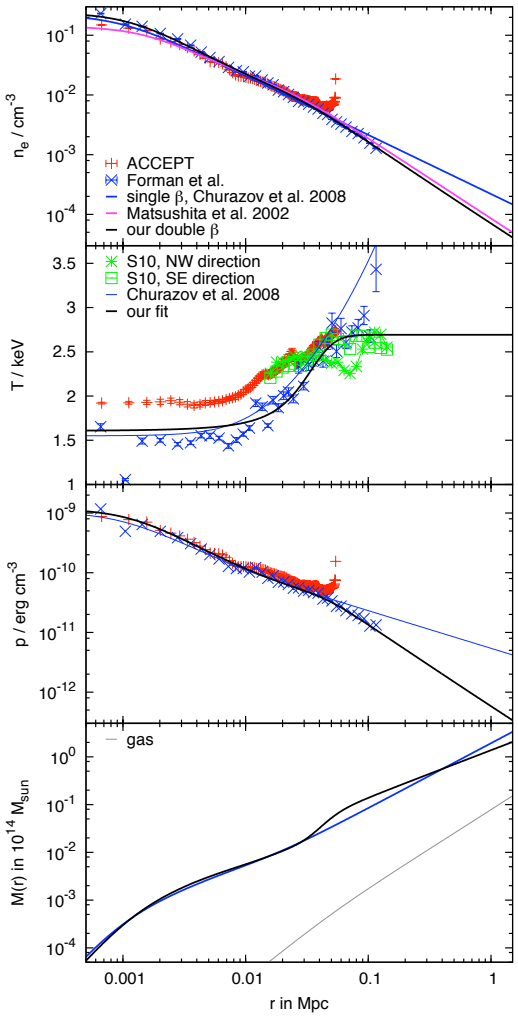

Figure 2. Overview of the Virgo cluster model, comparison with observations: Panels show electron density, temperature, pressure, and cumulative mass. For details see Sect. 2.4.1.

Table 2. ICM parameters for the Virgo cluster model.

density:	double beta profile	
core radii $r_{1,2}$/ kpc:	1.20	23.68
core densities $\rho_{01,02}/(\mathrm{g\,cm^{-3}})$:	$4.42 \cdot 10^{-25}$	$1.38 \cdot 10^{-26}$
$\beta_{1,2}$:	0.42	0.52
temperature:	see Eqn. 1	
slopes $m_{1,2}/(\mathrm{K\,pc^{-1}})$:	-5.6	0.
$T_{01,02}/(10^7\,\mathrm{K})$:	1.78	3.12
break radius r_{break}/ kpc:	27.7	
break range a_{break}/ kpc:	10	

We study two different initial metal distributions, a steep and a flatter one, which are described in Sect. 5.1.

2.4.2 Subcluster

The gravitational potential of our subclusters is modelled by a Hernquist halo (Hernquist 1990).

We vary the mass and size of the disturber between 0.5 and $4 \cdot 10^{13} M_{\odot}$ and 50 and 200 kpc, respectively. At the upper end of our mass range, we are restricted by the condition that we want to model minor mergers only. A mass of $4 \cdot 10^{13} M_{\odot}$ equals the mass of the inner 300 kpc of Virgo. Hence, an interaction with higher mass subclusters would not be a minor merger any more and would leave obvious imprints in the Virgo cluster, which are not found. The lower end of the mass range is determined such that the subcluster still leaves an imprint that is comparable to the observations.

We abbreviate the combinations of subcluster mass and size and the pericentre distance of its orbit as MXaYdmin$Z$, where "MX" shall indicate a subcluster mass of $X \cdot 10^{13} M_{\odot}$, a$Y$ a scale radius of Y kpc, and dmin$Z$ a pericentre distance of Z kpc. E.g. in our fiducial run, M2a100dmin100, a subcluster with $2 \cdot 10^{13} M_{\odot}$ and scale radius 100 kpc passes the cluster centre with a minimal distance of 100 kpc.

2.4.3 Orbits

The orbit of the subcluster can influence the intensity and duration of the impact on the ICM. The smaller the pericentre distance of the subcluster orbit, the stronger the impact on the central gas should be. Faster subclusters spend less time near the cluster centre and thus should cause less perturbation. We test these expectations by modelling the passage of the subcluster along different orbits. The characteristics of these orbits are summarised in Fig. 3. We study orbits with pericentre distances, $d_{\rm min}$, of 20, 100, 200, and 400 kpc. We construct two groups of orbits: a group of "slow" orbits, where the subcluster moves subsonically at distances larger than ~ 500 kpc; and a group of fast orbits, where the subcluster moves supersonically even outside a few Mpc, and consequently also moves faster through the cluster centre. The slow orbits are shown by thick lines in Fig. 3, they are labelled and colour-coded by their pericentre distance. The fast orbits are represented by thin lines.

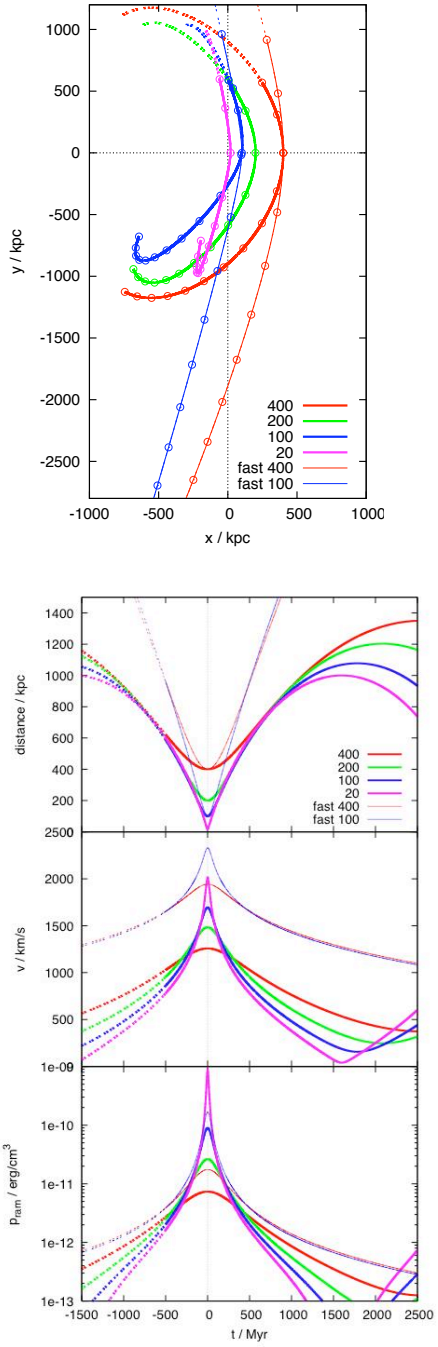

Figure 3. Different orbits of the subcluster: The top figure displays the orbits in the xy-plane. Different colours denote different pericentre distances (given in legend, in kpc). The thin lines are for faster orbits, thick lines for slower ones. The circles along the orbit are spaced by 250 Myr. We start our simulations in the "upper" ($+y$-direction) part of the orbital plane, where the dashed lines switch over to solid lines. The bottom figure displays the evolution of distance to the cluster centre, total velocity, and ram pressure as a function of time for each orbit.

3 EVOLUTION AND DYNAMICS OF SLOSHING IN VIRGO

We demonstrate the evolution of the gas sloshing in Fig. 4, which displays the ICM temperature (colour coded) and velocity field (white arrows) of the ICM in the orbital plane at different timesteps. The sloshing proceeds very similar to the scenario explained in Sect. 1.1: At core passage, the central cool ICM is offset due to the gravitational pull of the subcluster. The subsequent sloshing is a superposition of linear sloshing and circular motion, leading to the formation of a cool spiral pattern and CFs. The only effect not mentioned there is the adiabatic heating due to infall of ICM into the subcluster potential: The initially hydrostatic ICM of the Virgo cluster starts moving slowly towards the subcluster right from the start of the simulation (see top panel

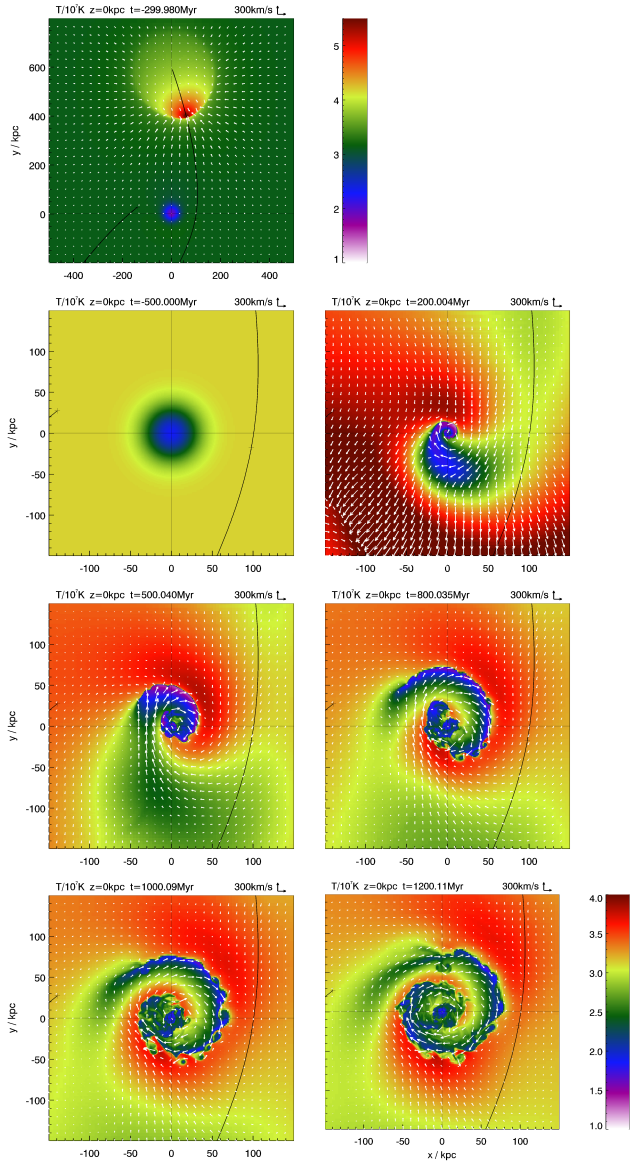

Figure 4. Time series of temperature slices, taken in the orbital plane of the subcluster. White arrows indicate the velocity field, colours code the ICM temperature in 10^7 K. The series is for the fiducial run M2a100dmin100. The time is noted in the title of each frame, so is a scale bar for the velocity vectors. The top panel shows a large-scale view 0.4 Gyr prior to pericentre passage. The remaining panels focus on the central 150 kpc. They share the temperature colour scale in the bottom left.

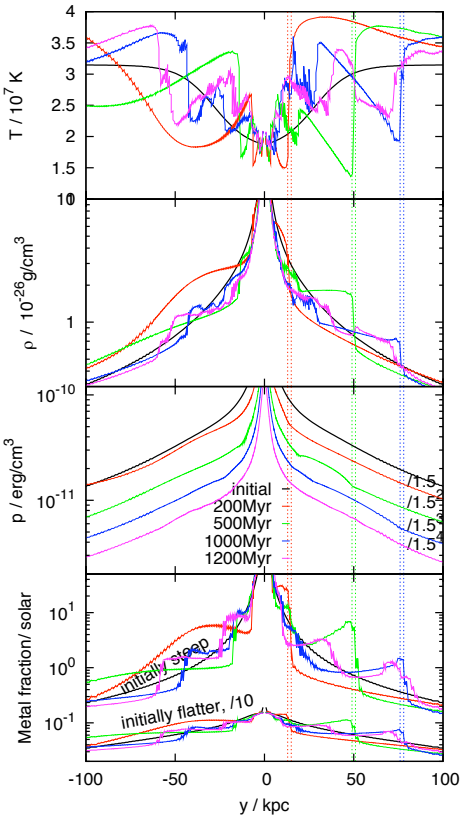

Figure 5. Profiles of temperature, density, pressure, and metal fraction along the y-axis, at different timesteps (colour-coded). For clarity, the pressure profiles of different timesteps are divided by 1.5, 1.5^2, 1.5^3, 1.5^4. For metallicity, we show two sets of profiles for two different initial metal distributions (see Sect. 5.1). In the upper set of profiles, the initial metal density is proportional to the light profile of M87, for the lower set of profiles, the initial metal density profile is flatter. The whole set of flatter profiles is divided by a factor of 10 to avoid confusion. On the "upper" side ($+y$-direction), we mark the outer CF by a thin vertical doublet line of the colour matching the legend.

in Fig. 4). The ICM near the position of subcluster starts falling into the subcluster potential well and heats up by adiabatic compression, leading to a heated region following the subcluster along its orbit.

Qualitatively, the evolution is independent of subcluster and orbit characteristics. Subcluster mass, size, and orbit mainly influence the intensity of the contrast of density and temperature across the CFs. The influence of these parameters is discussed in detail in Sect. 4.

Despite the rigid potential approximation, the evolution in our simulations is similar to the one described in simulations with dynamic DM (AM06, ZuHone et al. 2010). Both, AM06 and ZuHone et al. (2010), report that occasionally the cool central gas is separated from the central DM peak completely by a few kpc before falling back. In Virgo, there is never a complete separation of the cool core from the very centre because the central potential well is so steep.

In Fig. 5 we take a closer look at the structure of the cool spiral and CFs by plotting temperature, density and pressure profiles along the y-axis. The CFs are indeed discontinuities in temperature and density within our resolution (1-2 kpc), but the pressure is continuous. However, the pressure gradient shows a discontinuity just inside each CF, which decreases with time. Inside of each CF, there is a plateau in density accompanied by an increasing temperature towards smaller radii because the cool gas from the centre has been moved outwards. Going further inwards, in many profiles the next CF can be detected. The metal profiles will be discussed in detail in Sect. 5.

The typical velocities induced by sloshing in our fiducial

model are 200 to 300 km s^{-1}, which is about half the circular velocity inside the inner 30 kpc of the Virgo cluster. This supports the idea of Keshet et al. (2009), that the circular component of the sloshing motions contributes a significant radial acceleration working on the sloshing gas in the form of centripetal acceleration.

4 COMPARISON WITH OBSERVATIONS

In this section, we give a detailed comparison between observed and simulated characteristics of the CFs in the Virgo cluster. We first introduce our synthetic observations. Then we discuss evidence that in Virgo indeed the gravitationally induced sloshing scenario took place. Next, we derive the LOS, the age, and constrain the subcluster and orbit characteristics. As the representative case, we describe the observational features for the fiducial run M2a100dmin100 (see Sect. 2.4.2).

Along with the one-to-one comparison to Virgo, we also apply our results to other CF clusters.

4.1 Preparation of synthetic observations

The observations of the Virgo cluster (Sect. 1.3) provide an X-ray image, brightness residual maps, and profiles of X-ray brightness, projected temperature, and projected metallicity across the NW and SE cold front, averaged over 90^o. Further desirable data would be a complete temperature and metallicity map. In order to compare our results to the observation, we produce all these images and profiles from our simulations. In order to highlight the simulation results, e.g., regarding the width of the CFs, we do not convolve our maps with an instrument kernel, nor do we reduce the resolution of our maps to match current observations. Consequently, especially our temperature maps have a higher spatial resolution than currently available.

4.1.1 X-ray images

In Fig. 6, we show the observed X-ray image (top left), and a time series of synthetic X-ray images of the inner 125 kpc of the simulated cluster for our fiducial run. The synthetic images are derived by projecting $n^2\sqrt{T}$ (where n is the particle density and T the gas temperature) along the LOS. This results in unnormalised brightness images. The top right image displays the initial state of the cluster. In subsequent rows, we show X-ray images at $t = 0.5, 1, 1.2$ Gyr for two LOSs: perpendicular to the orbital plane (along z-axis, lhs) and parallel to the orbital plane (along x-axis, rhs).

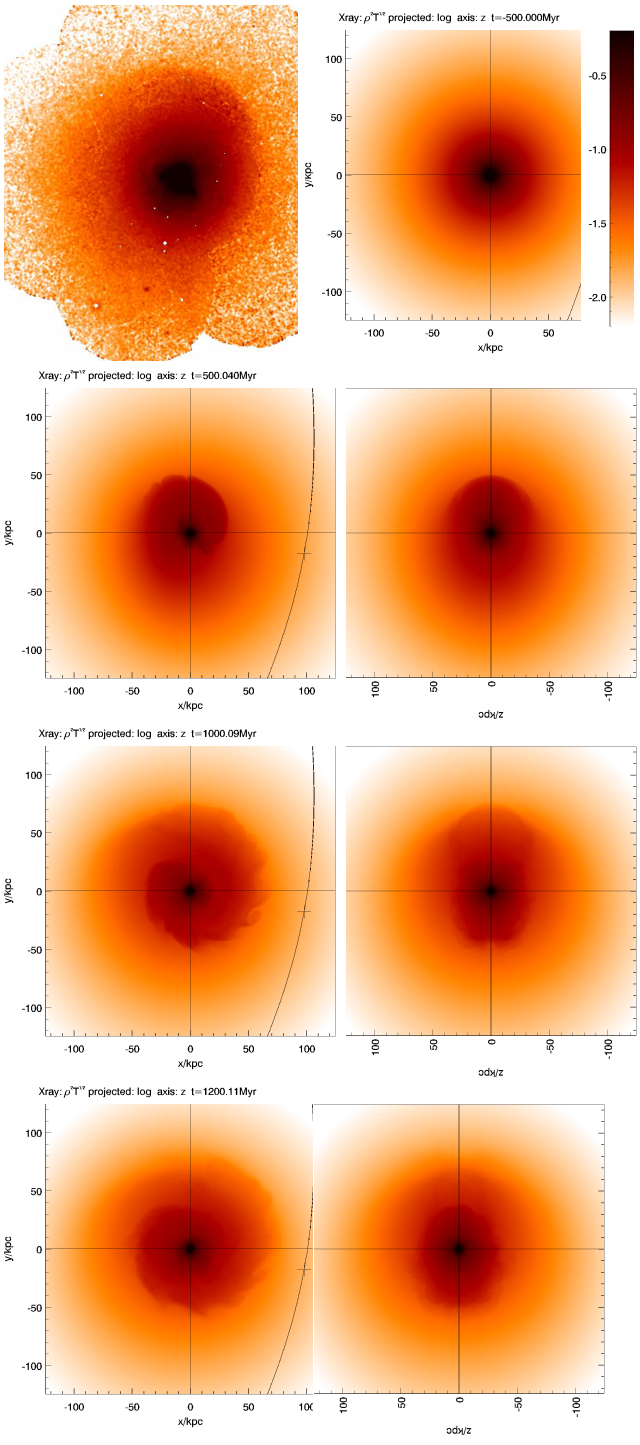

Figure 6. Observed X-ray image (top left, same as in S10, but consistent colour scale), and a time series of synthetic X-ray images of the inner 125 kpc for our fiducial run. The top right image displays the initial state of the cluster. In subsequent rows, we show X-ray images at $t = 0.5, 1, 1.2$ Gyr for two LOSs: perpendicular to the orbital plane (along z-axis, lhs) and parallel to the orbital plane (along x-axis, rhs). The brightness is given in arbitrary units.

4.1.2 Brightness residual maps

Brightness residual maps, or residual maps for short, are used to enhance the contrast of the X-ray images: We divide each X-ray image by its azimuthal average. We favour this version over residuals w.r.t. a fitted β-model because we want to highlight the deviation from the initial symmetry. Figure 7 displays the residual maps corresponding to the second and fourth row of Fig. 6.

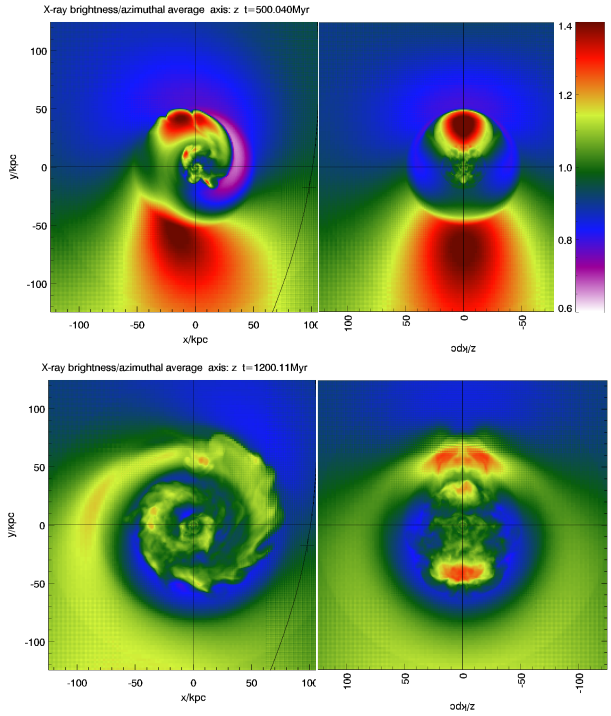

Figure 7. Time series of residual maps for fiducial run: dividing X-ray brightness image by azimuthally averaged X-ray brightness. Left: LOS perpendicular to orbital plane, along z-axis of simulation grid. Right: LOS parallel to orbital plane, along x-axis of simulation grid. For $t = 0.5\,\mathrm{Gyr}$ (upper row) and $t = 1.2\,\mathrm{Gyr}$ (bottom row).

4.1.3 Projected temperature

Reducing the 3D temperature structure of a galaxy cluster to 2D map requires averaging along the LOS for each pixel of the temperature map. Each grid cell along the LOS may contribute to this average with a different weight. A standard way is to calculate the emission-weighted projected temperature:

$$T_{\mathrm{ew}} = \frac{\int W\,T dz}{\int W dz} \quad \text{with} \quad W = n^2\sqrt{T} \tag{2}$$

Mazzotta et al. (2004) show that using the weights

$$W = n^2/T^{3/4} \tag{3}$$

results in estimates for projected temperature which are closer to the value derived by spectroscopical temperature fitting. Using this weighting scheme, Fig. 8 shows projected temperature maps along two LOSs (first 2 rows). For comparison, the bottom left panel of Fig. 8 repeats one temperature map but with emission-weighted projection. The bottom right panel displays the initial state.

4.1.4 Profiles

Azimuthally averaged profiles across CFs of projected quantities are shown in Fig. 9. The profiles shown here are taken from maps projected along the LOS perpendicular to the orbital plane of the subcluster (z-axis of the grid). We average the profiles over an azimuthal range of 90^o, as in the

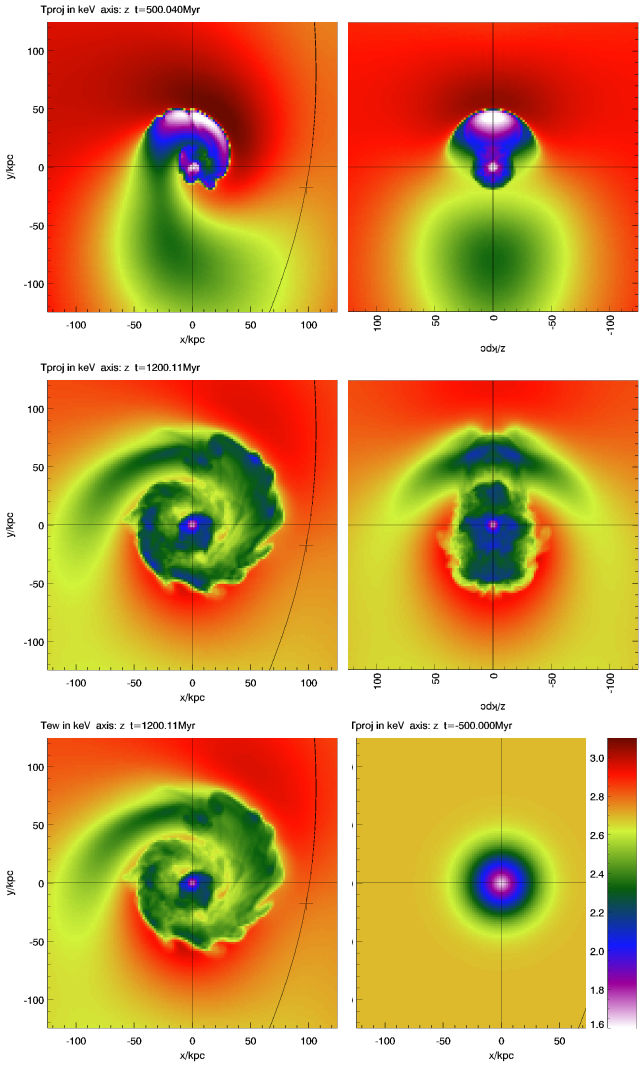

Figure 8. Projected temperature maps for fiducial run, using projection scheme of Mazzotta et al. (2004) (top and middle row, for $t = 0.5\,\mathrm{Gyr}$ and $1.2\,\mathrm{Gyr}$, respectively). The lhs of these rows shows the projection along the LOS perpendicular to the orbital plane, along the z-axis of the simulation grid. The rhs panels are for projection along the LOS parallel to the orbital plane, along the x-axis of the grid.
For comparison, the bottom left panel repeats the temperature map for $t = 1.2\,\mathrm{Gyr}$, but with emission-weighted projected temperature. The bottom-right panel shows the initial temperature distribution and the colour scale.

observations. For the NW CF, we average between $+x$-and $+y$-axis, for the SE CF, we average between $-x$- and $-y$-axis. For comparison, we also show the observed profiles. Profiles taken for projections along the grid x-axis (LOS parallel to orbital plane) are very similar.

4.2 Basic evidence for sloshing scenario

4.2.1 Brightness and temperature edges

The basic evidence for gas sloshing in Virgo is formed by the existence of a pair of brightness discontinuities in X-ray images at about 90 kpc NW and 30 kpc SE of the cluster

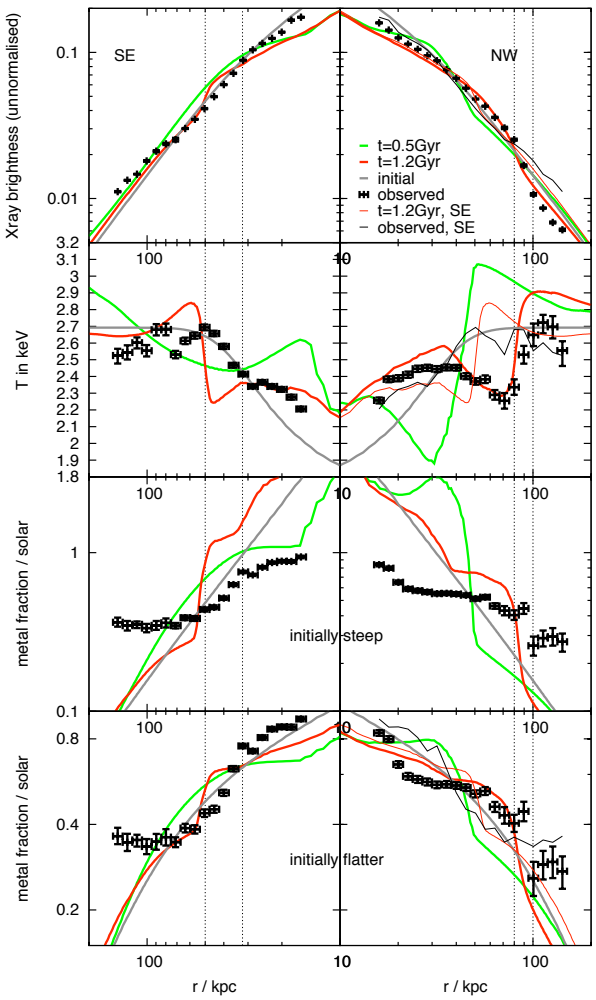

Figure 9. Azimuthally averaged profiles of X-ray brightness, projected temperature, and projected metallicity for fiducial run, for two timesteps (thick green and red lines, see legend). The LOS is perpendicular to orbital plane, along the grid's z-axis. The rhs column is for the NW direction, the lhs column for the SE direction.
The observed, also azimuthally averaged profiles are shown as black points with error bars (Simionescu et al. 2010).
For the metallicity we show the evolution for two initially different metal distributions: In the third row, the initial metal density follows the light profile of M87. In the 4th row, the initial metal distribution is flatter (see Sect. 5.1).
In order to demonstrate the alternating behaviour of the profiles discussed in Sect. 4.5.3, we repeat the observed and simulated SE profiles for $t = 1.2$ Gyr as thin lines in the rhs column.
The dashed vertical lines mark the position of the observed CFs.

centre (see Sect. 1.3). In the simulations, a surface brightness discontinuity towards the N of the cluster core appears nearly immediately after the subcluster passed the cluster core (Fig. 6). A second front towards the S at a smaller radius becomes evident after 600 Myr. With time, the edges move outwards. The edges are seen more clearly in the residual maps (Fig. 7).

For being a cold front, the brightness edge needs to be accompanied by a temperature discontinuity in the sense that the X-ray brighter side is the cooler one. For the Virgo cluster, no temperature map is available, but the observed profiles across the edges (Fig. 9) show a temperature discontinuity at the position of the X-ray brightness discontinuity in this sense. The synthetic projected temperature maps clearly show temperature discontinuities at the same positions as the X-ray brightness edges, with the brighter side being the cooler one, independent of the weighting scheme.

Thus, the basic characteristic of the sloshing CFs, namely a downward X-ray brightness jump accompanied by an upward temperature jump with increasing radius, are found in simulations and observations.

4.2.2 Cool structures and brightness excess structures spatially consistent

In addition to the actual edges in projected temperature, the projected temperature maps for the LOS perpendicular to the subcluster orbital plane in Fig. 8 reveal a cool spiral-shaped region in the cluster centre. The outer edge of this cool spiral is the actual cool front. The exact temperature structure within the cool spiral depends somewhat on the projection scheme used: The cool spiral is somewhat cooler in the Mazzotta weighting scheme. There tends to be a cooler outer rim just at the edge of the fronts, which is less pronounced in the emission-weighted temperature maps. This difference is the same as reported in Mazzotta et al. (2004): In their weighting scheme, cool regions tend to be somewhat cooler than in emission-weighted temperature maps. The temperature maps derived by the Mazzotta weighting resemble the actual structure of the CFs as seen in the temperature slices (Fig. 4) better.

If the cluster is seen along a LOS parallel to the orbital plane, there are cool arc-like structures N and S of the cluster centre, whose outer edge are the actual CF. The same structures appear, spatially consistent, as a brightness excess in the residual maps shown in Fig. 7.

These spiral- or arc-shaped brightness excess features are the most easily detectable signatures of ICM sloshing. They can be detected even with poor resolution, when the fronts themselves are smeared out. The morphology of the excess structure (spiral or arcs) may also be more easily detected than the one of the edges themselves.

AM06 have shown the cool spiral- or arc-like structures caused by sloshing, along with spiral- or arc-like fronts in synthetic X-ray images. Our work shows that these cool structures are perfectly spatially consistent with brightness excess features in residual maps. The temperature and metallicity maps of the inner 70 kpc of the Virgo cluster (Simionescu et al. 2007) show the same correspondence to the residual maps (Fig. 1) around the SE front.

This correspondence of brightness excess and cool regions is found in all known sloshing CF clusters where both data sets exist.

4.3 Morphology and orientation of Line-of-Sight (LOS)

Two types of arrangements of sloshing CFs are known: Either the CFs trace a spiral, or they form arcs on opposite sides of the cluster core. The first case is expected if our LOS

is perpendicular to the orbital plane of the subcluster, the second, if we see the orbital plane edge-on (AM06). Moreover, the morphology of the cool brightness excess regions described in the previous section (Sect. 4.2.2) follows the same dependency on the LOS. Our simulations confirm this result (see Figs. 7, 8).

The only maps available for the Virgo cluster so far are the residual maps presented in Fig. 1 (S10). We have shown that the morphology of this map depends to some degree on the method of its generation. However, a spiral morphology of both, the brightness excess region and the fronts themselves, is clearly seen in the map showing residuals w.r.t. azimuthal symmetry. The map showing residuals w.r.t. a β-model also shows a hint of a spiral, and so does the X-ray image (S10). Hence, we conclude that our LOS towards the Virgo cluster is approximately perpendicular to the orbital plane of the responsible subcluster. It is not possible to put clear constraints on the orientation on the LOS because the dynamical Virgo cluster very likely experienced additional processes that modified its symmetry.

We note that we detect the CFs in projections along all grid axes, which was also shown by AM06. Hence, contrary to what was claimed by Birnboim et al. (2010), the detection of sloshing CFs in a given cluster does not require a favourable viewing angle.

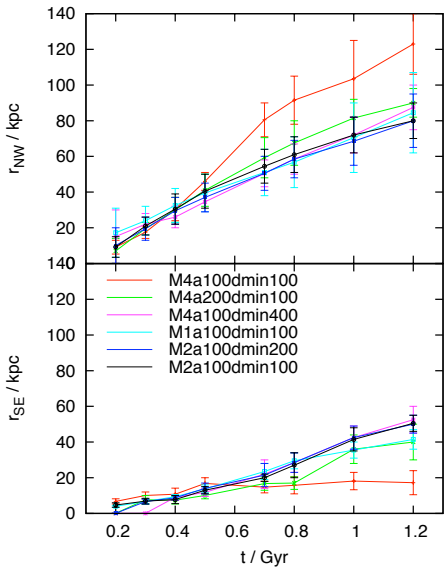

Figure 10. Radius of the NW (top panel) and SE (bottom panel) cold front as a function of time, for different parameter sets, see legend. The error bars indicate the width of the fronts derived from azimuthally averaged temperature profiles (compare Fig. 9).

4.4 Radius of the CFs and their age

In Sect. 4.5.2 we show that the "edge" of the NW CF in the observed profiles (Fig. 9) is not the jump between the two data points next to 90 kpc, but is smeared out between 80 and 100 kpc. Analogously, for the SE front we derive a cluster-centric distance between 32 and 50 kpc. The results of taking the same measurement for the simulation at $t = 1$ Gyr and 1.2 Gyr, are summarised in Table 3. Given the simplicity of our model, the radii of both, the NW and SE CF, agree remarkably well between observations and simulations between $t = 1$ Gyr and 1.2 Gyr. Hence, the age of the system of CFs in Virgo is about 1-1.2 Gyr, where age is defined as the time passed since the subcluster's pericentre passage. This doubles the estimate derived in S10.

At a given time, the CF radii are nearly independent of subcluster mass, size and orbit (Fig. 10). Only in run M4a100dmin100, which is close to a major merger, and the rather massive subcluster is close to disrupting the cool core, the radii of the CFs show a significant deviation. The sloshing itself is governed by the underlying potential of the Virgo cluster. Thus, the distance of the CFs from the cluster centre depends mainly on their age, which we derived above. Subcluster mass, size and orbit influence the amplitude of the initial perturbation in the ICM, and thus the contrasts across the fronts.

We note that the three-dimensional topology of the cool structure induced by the sloshing approximately encompasses a thick disk with thickness ± 35 kpc along the z-direction and an extent in the xy-plane as shown in Fig. 4. Hence the radius of the CFs would not be shortened significantly along any LOS.

4.5 Principal structure of evolved CFs

We have derived the age of the Virgo CFs to be 1-1.2 Gyr in Sect. 4.4. From now on, we concentrate on the CFs at that stage in our simulation, and compare them to the observation.

4.5.1 Profiles

Radial profiles taken towards the CFs (see Fig. 9) show a consistent structure in both, simulations and observations:

- Starting from the cluster centre, the temperature increases with increasing radius, while X-ray brightness and metallicity decrease.
- With increasing radius, when approaching the CF, the temperature decreases or forms a plateau. Also the metallicity shows a plateau.
- The front itself is manifested as a steep increase in temperature, a steep decrease in metallicity and X-ray brightness. The width of the CFs is discussed in Sect. 4.5.2.
- Outside the CF, the temperature again decreases somewhat, i.e. there is a warmer rim enclosing each CF.

The same structure is found in other CF clusters, as far as the data quality allows. The decrease of temperature with radius inside the CFs may be a speciality of the compactness of the Virgo cluster, but plateaus in temperature inside the CF are found for the N front in A496 (Dupke et al. 2007), the SW front 2A 0335+096 (Sanders et al. 2009a), A1795 (Markevitch et al. 2001), A2142 (Markevitch et al. 2000), A2204 (Sanders et al. 2005), MS 1455.0+2232 (Mazzotta & Giacintucci 2008), NE front in NGC5098 (Randall et al. 2009), probably in A1201 (Owers et al. 2009). A metallicity plateau is seen in A2204 (Sanders et al. 2009b). Indications

Table 3. Quantitative characteristics of observed and simulated CFs.

	NW			SE		
quantity	observation	sim $t = 1\,\mathrm{Gyr}$	sim $t = 1.2\,\mathrm{Gyr}$	observation	sim $t = 1\,\mathrm{Gyr}$	sim $t = 1.2\,\mathrm{Gyr}$
radius in kpc	80-100	62-82	70-90	32-50	38-48	46-55
X-ray brightness jump	2.3	1.8	2.1	2.1	1.9	1.8
Temperature jump	1.08-1.19	1.34	1.27	1.15	2.26	2.26
Metallicity jump	1.15-2.	2	1.9	1.5-1.8	1.5	1.6

of a warm rim outside the CF are seen in A1795, A2204 and A2142. However, most published data does not resolve the temperature profiles well enough to clearly detect these features. Occasionally, only the temperature jump across the CF is measured.

For future observations we suggest to derive the full profiles from the cluster centre beyond the CFs. This will enable a better comparison to simulations, and tighter constraints on the identification of the responsible subcluster.

4.5.2 The width of CFs

In X-ray images, the brightness edges at the CFs are unresolved and are usually interpreted as a discontinuity. The same is true for azimuthally averaged profiles, if the average is taken over a small angle only. In case of the average over 90^o used in Virgo, the averaging smoothed out the edges in the profiles in both, the observation and the simulation, in all quantities, for the NW and the SE side. We mark the width of the observed CFs by dotted vertical lines in Fig. 9. The only exception is the observed metallicity profile across the NW CF, where it exhibits a sharp jump between neighbouring data points, while X-ray and temperature do not. We therefore suspect that the last data point inside the NW front is flawed by the multi-temperature structure in this bin.

For an optimal measurement of the CF width and the contrasts across it, we suggest to arrange the spectral extraction regions next to the front such that their borders follow the front as closely as possible.

4.5.3 Alternating structure of cool+brightness excess and warm+brightness deficit

Along both LOSs, the simulated residual maps and temperature maps show a characteristic staggered pattern of cool brightness excess and warm brightness deficit (Figs. 7 and 8). Outside both CFs, there is a region of enhanced temperature combined with brightness deficit. Thus, the typical feature produced by gas sloshing is not only a spiral- or arc-like brightness excess, spatially consistent with a cool feature, but a staggered distribution of cool brightness excess regions and warm brightness deficit regions. If seen perpendicular to the orbital plane of the subcluster, there is a cool excess spiral wrapped inside a warm deficit spiral; if the orbital plane is seen edge-on, the cluster exhibits cool excess arcs bordered by warm deficit arcs. The same pattern appears in the Virgo cluster (Fig. 1).

This alternating behaviour continues even to larger radii: Outside the outer CF (towards NW/N), there is always a large deficit region. On the southern side, outside the deficit region enclosing the southern CF, there is an extended excess region. Also this feature is found in simulations and in observation.

The same feature is evident in the profiles: When both, NW and SE profiles are plotted in the same panel, they show a characteristic alternating behaviour, which we demonstrate by overplotting the SE profiles with thin lines on the NW side in Fig. 9 (observed by thin black, simulated at $t = 1\,\mathrm{Gyr}$ in thin red). At the innermost radii, the X-ray brightness and metallicity are higher on the SE side, whereas the temperature on the SE is lower. At the radius of the SE CF, both sides change: now the X-ray brightness and metallicity are higher at the NW side, and the temperature is lower. At the radius of the NW CF, the sides switch again.

This alternation is found in all simulations. The contrast between the opposite sides increases for subclusters with deeper potential wells.

This staggered pattern is also observed in other clusters (for references see Sect. 4.5.1): A496, A2142, MS 1455.0+2232, RX J1720.1+2638 (Mazzotta & Giacintucci 2008).

4.6 Asymmetry on large scale

In addition to looking at the central part of the simulated Virgo cluster, we also present synthetic observations out to a radius of $\sim 0.5\,\mathrm{Mpc}$. At first glance, the large-scale X-ray images appear approximately symmetrical and undisturbed as soon as the subcluster has left the field of view (see Fig. 11, top row). Except for the central spiral excess, there is no obvious trace of the interaction. The residual maps, however, (Fig. 11, bottom row) reveal that there is a clear asymmetry in the X-ray brightness in the sense that after pericentre passage, the brightness is enhanced along the outgoing orbit of the subcluster, i.e., towards the direction of the subcluster after core passage.

The observed residual map of Virgo extends to about 150 kpc. Inside this range, it agrees with the predicted asymmetry: Outside the NW CF, there is mainly a brightness deficit w.r.t. the azimuthal average. In contrast, there is a clear brightness excess region at the southern edge of the residual map. It will be interesting to compare our prediction to deep larger-scale observations. The observational detection of such a large-scale feature would greatly help to identify the subcluster responsible for the CFs, because it points towards its current position. However, Virgo is a dynamical cluster, still in the state of assembly, so that also other processes will influence the symmetry or asymmetry at this length scale. Moreover, if the subcluster moves along an orbit with a larger impact parameter, d_{min}, the enhance-

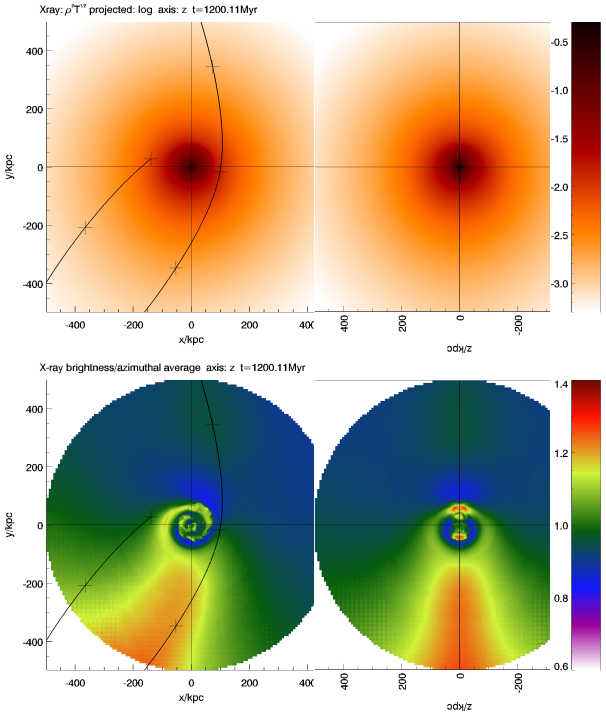

Figure 11. Synthetic X-ray brightness maps (top row, arbitrary units) and residual maps (bottom row) for large field of view (out to 500 kpc) at $t = 1.2$ Gyr. The lhs panels are for LOS perpendicular to orbital plane, the rhs for LOS parallel to orbital plane. The black line marks the subcluster orbit. The crosses along the orbit are spaced by 0.25 Gyr.

ment in brightness towards south is more spread (Fig. 12, bottom row), making it more difficult to trace the responsible subcluster. Also for the fast subcluster, the enhancement of the outgoing orbit is less pronounced.

Similar large-scale features in residual maps and even temperature maps are seen in other sloshing CF clusters: the cluster 2A 0335+096 (Tanaka et al. 2006) shows a brightness excess towards SE and NW, accompanied by a large cool region towards SE. This could well be the continuation of the central cool spiral seen by Sanders et al. (2009a). Hence the responsible subcluster should have moved towards SE. Tanaka et al. (2006) discuss cooling or ram pressure stripping or turbulent viscous stripping as the origin of this cool brightness excess region. Our simulations suggest that it is a by-product of the passage of a subcluster that was already stripped before pericentre passage.

The cluster A496 (again Tanaka et al. 2006) shows a clear brightness excess (and also cooler) region ~ 400 kpc towards NW, from which the authors derive that the subcluster passed the main cluster core from NW to SE. Our simulations show that indeed the opposite happened. This excess region does not seem to match the orientation of the central CFs described in Dupke et al. (2007). However, Tanaka et al. (2006) report an additional CF about 200 kpc SE of the cluster centre, which is evident as a brightness excess region in their residual map. This seems to be the outermost CF, which now is opposite of the large-scale excess region. The central CFs discussed in Dupke et al. (2007) are the second, third, and maybe fourth CF in this cluster. Apparently, A496 possesses a well-organised set of CFs, indicating a late stage of sloshing. This cluster will be an interesting target for future simulations.

The residual and temperature maps for the Perseus cluster (Churazov et al. 2003) qualitatively show exactly the same features: a cool brightness excess at large radius towards E, while the outmost CF is towards W.

Also in this large-scale structure, there is the coincidence of brightness excess and cooler temperature. We also find this in our simulations. The strength of the feature would, however, depend on the mass of the outgoing subcluster, hence it needs to be confirmed with hydro+N-body simulations. The fact that it is found in real clusters is encouraging.

The detection of this large-scale asymmetry also favours the standard sloshing scenario over the core oscillations scenario, which should leave traces in the cluster centres only.

4.7 Contrasts across the edges and subcluster mass/size/orbit

4.7.1 Best-matching, fiducial case

Often, the contrast across a CF is measured as the jump between two neighbouring pixels, which exhibit the strongest gradient. However, as discussed above, the width of the CFs is smeared out by the azimuthal averaging. Hence, the contrast across the CF is the ratio of the value at the inner and outer range of the CF radius given in Table 3. The values derived in this manner from the observation as well as the simulation are also listed in Table 3. We suggest that in observations, the rings for profile deduction should be taken such that they follow CFs, which is not necessarily centred on cluster centre. We expect a higher contrast between neighbouring data points just inside and outside of the CF, and a more precise position of CFs.

The contrast of X-ray brightness and temperature across the CFs depends on their age and on the subcluster characteristics. With time, the CFs move outwards, and the contrast of all quantities across them decreases. The age of the CFs is already fixed by their radius, so the contrast can be used to derive the subcluster characteristics. In brief, subclusters with deeper potentials (more massive or more compact) cause higher contrasts, i.e. more intense CFs.

In our fiducial model, the contrasts in X-ray brightness and projected temperatures agree approximately with the observed values (see Table 3). X-ray contrast a bit too weak, the temperature contrast a bit too high, the metal jump about right if flatter initial metal distribution is used (see Sect. 5). Given that the metallicity contrast across the CF depends strongly on the initial (unknown) metal distribution, it is not straightforward to use the observed contrast as a constraint on sloshing dynamics. The agreement between simulation and observation is satisfactory for such a simple model.

The strongest discrepancy is in temperature. Both, the observed and the simulated value are projected temperatures, which are, however, derived in different ways. While simulated value comes from a weighted average along the LOS, the observed one results from a single-temperature fit ("spectroscopic temperature") to the spectrum averaged over an elliptical ring of 90° azimuthal length. Systematic

differences between both methods are partially responsible for the discrepancy. E.g., using emission-weighting instead of the weighting scheme of Mazzotta et al. (2004) for deriving the projected temperatures results in a smaller temperature contrast. However, Mazzotta et al. (2004) showed that their scheme gives projected temperatures closer to the spectroscopic temperature in the context of major cluster mergers. It has not yet been tested in the context of gas sloshing. Given that this scheme gives more weight to the cool gas, it may lead to an overestimate the temperature contrast. Deprojecting the observed temperature profile is in preparation (Forman et al.).

In the simulations, the temperature outside the CFs is somewhat higher than the observed one, because the simulations were initialised with the observed Virgo temperature profile. Shock-heating due to the moving subcluster causes the overall temperature to increase slightly. Initialising the simulations with a somewhat lower temperature could avoid this minor disagreement. However, we decided to initialise the simulations with the observed profiles in order to keep the initial model simple and comprehensible.

The fact that the X-ray jumps are too weak corresponds to fact that observed residual map shows higher contrast that predicted ones. The simulations consistently predict a brightness excess at the 10% level, whereas the observation shows an excess at the 30% level. Even with our most massive subcluster we did not reach this level. This might be due to the fact that the Virgo cluster is intrinsically slightly elliptical along the axis connecting the CFs (Simionescu et al. 2007), which enhances the deviations from azimuthal symmetry.

Our parameter study demonstrates that subclusters between the fiducial case ($2 \cdot 10^{13} M_\odot$ and scale radius 100 kpc, $d_{\rm min} = 100$ kpc) and a twice as massive subcluster of similar scale radius, which passes by at a larger distance of about 400 kpc, match the observational data equally well. We discuss this degeneracy in more detail in Sect. 4.8.

4.7.2 Excluded parameter space

In general, subclusters with shallower potentials and subclusters with larger pericentre distances cause less intense CFs, and vice versa. Thus, subclusters with insufficient mass or too large pericentre distance cause contrasts that are too weak, whereas clusters with too much mass or too small pericentre distances cause CFs that are too strong. Table 4 briefly summarises which combinations of parameters can be excluded by comparing the contrasts across the CFs to the observation. We can exclude subclusters less massive than $10^{13} M_\odot$, because the resulting cold fronts show too weak a contrast. Subclusters more massive than $4 \cdot 10^{13} M_\odot$ passing the Virgo core closer than ~ 200 kpc would leave contrasts that are too strong or even disrupt the cluster core. Near head-on encounters can also be excluded because they heat the cluster core too much and do not cause the spiral-like morphology in the residual map, independent of the LOS, because too little angular momentum is transferred.

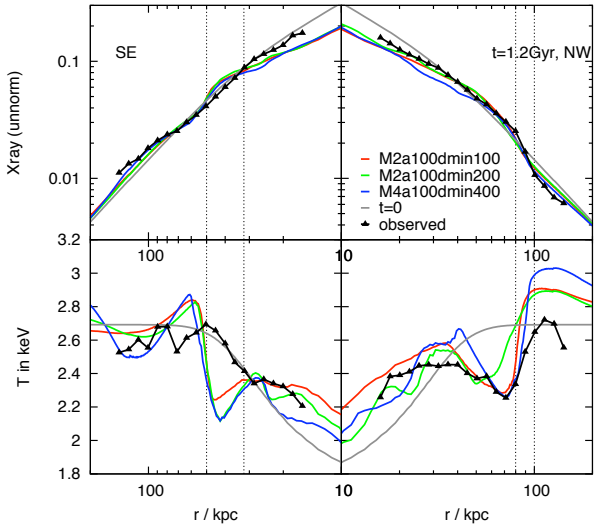

Figure 13. Comparison of azimuthally averaged profiles of X-ray brightness and projected temperature for best runs. See Sect. 4.8 for details. The cluster is seen perpendicular to the orbital plane. The thin vertical lines mark the observed CFs, same as in Fig. 9.

4.8 Degeneracy of subcluster+orbit characteristics

From our parameter study, we identified 3 sets of parameters that match current observation equally well: M2a100dmin100, M2a100dmin200, M4a100dmin400. Cases in between these cornerstones (e.g., $3 \cdot 10^{13} M_\odot$ and pericentre distance 300 kpc) are also possible. We compare our 3 best-fit runs in Figs. 12 and 13. The synthetic observations of these runs show remarkably little differences. E.g. we do not observe a tighter winding up of the cool/excess spiral with increasing $d_{\rm min}$.

Also the velocity of the subcluster does not introduce a major difference: We sent the fiducial subcluster M2a100 along the orbit "fast 100" (Fig. 3), i.e., also passing the Virgo cluster at 100 kpc distance, but about twice as fast. In the cluster centre, the resulting sloshing forms structures very similar to the fiducial run, with the contrasts across the CFs being slightly weaker. Hence, from the available observations, the velocity along the orbit is not well-constrained, neither is the current distance of the responsible subcluster to the Virgo centre.

4.8.1 Possibilities to distinguish between them in future observations

Distinguishing observationally between the proposed range of subcluster mass and pericentre distance is difficult. The best chance is to look at the large-scale asymmetry: A subcluster at the massive+large pericentre end of the range should leave a stronger imprint in the residual maps at large scales. In contrast, the fast interaction should leave a weaker imprint on the large scale. However, additional infall of subclusters or an intrinsic asymmetry would modify the large-scale feature, and could complicate the interpretation.

Table 4. Excluded parameter space: subcluster+orbit parameters of runs with insufficient agreement with observation. (1) Subcluster mass, (2) subcluster scale radius, (3) pericentre distance of orbit, (4) reason of mismatch.

$M_{\rm sub}/10^{13}M_\odot$	$a_{\rm sub}$/ kpc	$d_{\rm min}$/ kpc	comment
1	*	*	Contrast too weak, same holds true for less massive systems
2	100	20	Too much heating of inner 20 kpc due to strong impact on very central region
2	100	400	Contrast too weak, same true for similar mass and larger $d_{\rm min}$
2	200	100	Contrast too weak
4	100, 200	100	Contrast too strong. More massive subclusters at this $d_{\rm min}$ disrupt core.

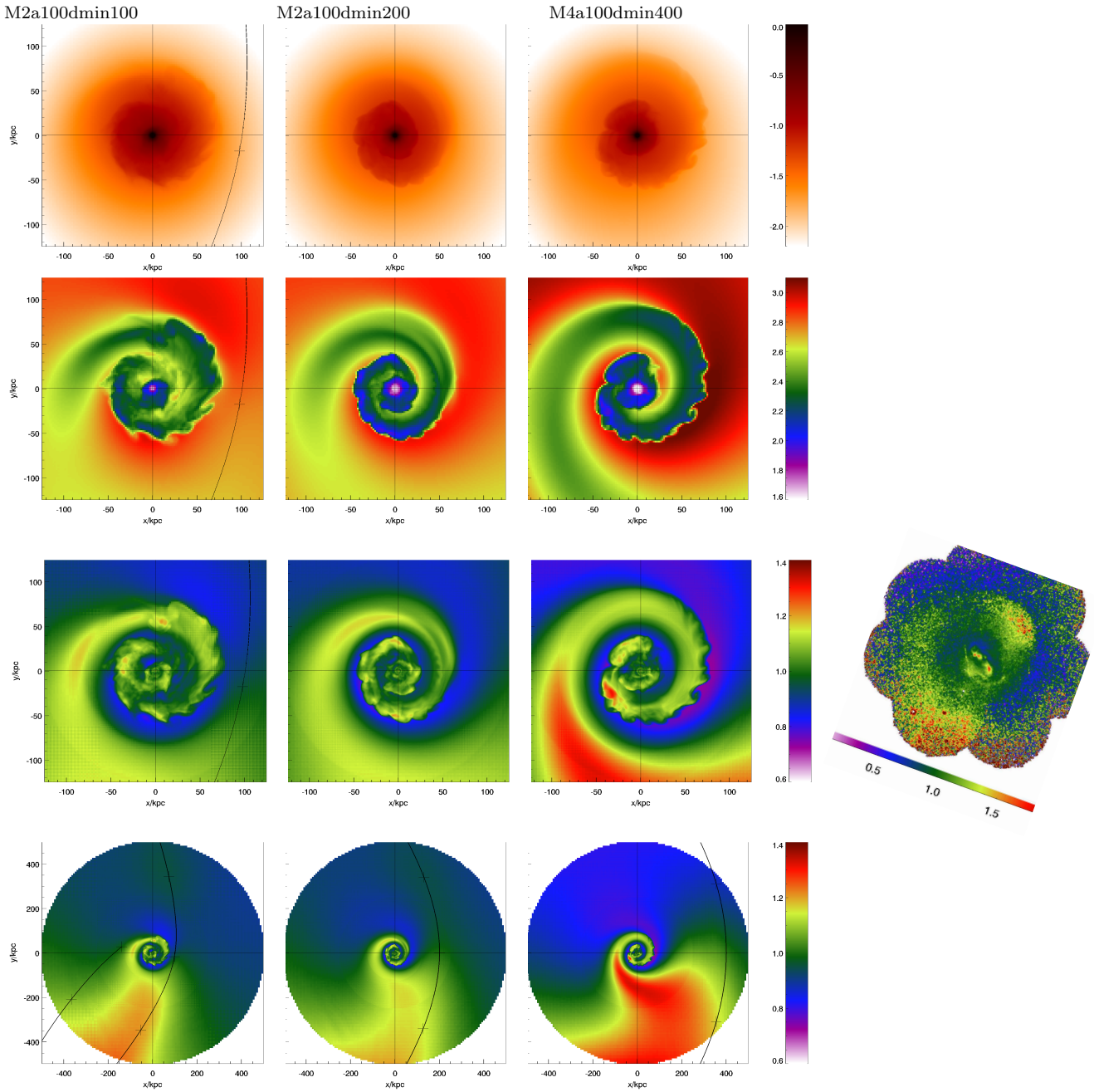

Figure 12. The three cases that fit observations best (columns, see label of run in top row): Comparing one quantity per row: synthetic X-ray image, projected temperature, residual map (for central region), and residual map for large field of view. We also show the observed residual map in the third row.

4.9 Identifying the responsible subcluster

The best alignment of the CF orientation between the observation and our simulations is achieved when we rotate our maps about 20^o anti-clockwise. Consequently, the current position of the subcluster (see position of subcluster at $t \approx 1\,\mathrm{Gyr}$ in Fig. 3 for different orbits) corresponds to about 1-2 Mpc S of the Virgo centre. The uncertainty in distance is due to the ill-constrained velocity of the subcluster. The subcluster should still be moving towards south.

The Virgo cluster catalogue (Binggeli et al. 1985, 1987, 1993) does not contain many bright galaxies in this region. The M49 group is in the correct position. Moreover, it contains ICM with a cool core of its own, and displays a brightness edge at its northern side and a tail at its southern side, indicating ram pressure stripping due to a significant motion towards north (Irwin & Sarazin 1996; Biller et al. 2004; Kraft et al. 2009). In contrast, we expect the responsible subcluster to be still moving towards S.

There are two spiral galaxies N4526 and N4535 about 400 kpc E of M49, but they differ in radial velocity by about $1400\,\mathrm{km\,s^{-1}}$, thus it is unlikely they form a group. Each of them alone is not likely to be massive enough.

The W group has a high radial velocity w.r.t. the Virgo mean, meaning it is a background group.

About 1 Mpc S of the Virgo centre there is the group of galaxies NGC 4424, 4442, 4445, which have comparable heliocentric velocities (350 to $530\,\mathrm{km\,s^{-1}}$). However, NGC 4424 has an HI tail pointing south, indicating ram pressure stripping due to a significant motion northwards, which contradicts our demands on the responsible subcluster.

The W' group (centred on elliptical NGC 4365) looks promising. It has a radial velocity comparable to the Virgo mean, and does not contain obvious ICM of its own. However, this group might be not massive enough. van den Bosch et al. (2008) give a total mass of NGC 4365 of $5 \cdot 10^{11} M_\odot$. According to Binggeli et al. (1993), the velocity dispersion of the W' group is about $300\,\mathrm{km\,s^{-1}}$. With a scale radius of 100 kpc this translates into a virial mass of about $2 \cdot 10^{12} M_\odot$. With a velocity dispersion of $400\,\mathrm{km\,s^{-1}}$ and scale radius 200 kpc, the virial mass would be $8 \cdot 10^{12} M_\odot$, which is still below the mass required for the responsible subcluster. Nonetheless, the W' group centred on NGC 4365, about 5^o (1.6 Mpc) S of the Virgo centre (about 500 kpc W-SW of M49) is the best candidate known to us.

5 METAL TRANSPORT

The observation of the Virgo core revealed that the cold fronts are associated with clear discontinuities/steep gradients in metallicity profiles. Sloshing redistributes the central gas, hence this process must also redistribute the heavy elements throughout the central region, very likely leading to metallicity edges coincident with the CFs. In addition to the edges, sloshing may also be able to broaden the metal distribution throughout the cluster centre.

We have studied the metal redistribution by gas sloshing in the Virgo cluster by tracing the evolution of an initially centrally peaked metallicity distribution. We find the evolution of the metal distribution to be tightly coupled to the overall dynamics. E.g. different setups that produce similar temperature structures, also produce similar metallicity structures, because both quantities undergo the same dynamical redistribution process.

Table 5. Parameters for deprojected Sersic profiles describing the steep (fitted to M87 light) and the flat metal distribution.

	steep ($\propto$ M87 light)	flat
scale radius	54.56 kpc	120 kpc
Sersic index	11.84	2

5.1 Initial metal distribution

We study two different initial metal distributions: an initially steep and a flatter radial metal density profile. In the steep case, the metal density follows the deprojected light profile of M87 (Kormendy et al. 2009). This follows the approach of Rebusco et al. (2006), who assume that originally the central metal distribution in a cluster follows the light profile of the central galaxy, but is broadened by a diffusion-like effect of gas turbulent motions. However, the central metal distribution may well have undergone other redistribution processes in the recent Gyrs (buoyant AGN inflated bubbles, turbulence), so that it is not clear that the initial distribution at the start of our simulations has to be proportional to the stellar mass. Hence, we consider a second case with a flatter initial metal profile, chosen as an approximate fit to the observed metal density inside the NW CF. In both cases, we fit the initial metal density distribution by a deprojected Sersic profile (Sersic 1963; van de Ven et al. 2009; Ciotti, L. & Bertin 1999; Prugniel, P. & Simien 1997). The parameters for both metal density distributions are listed in Table 5.

5.2 Evolution

The bottom panel of Fig. 5 displays the initial distribution and evolution of the metallicity along the grid y-axis, respectively. The profiles for the steep and the flatter case are compared in the same panel. To avoid confusion, the profiles for the flatter case are divided by a factor of 10. Qualitatively, the evolution of the metallicity profile is similar to the evolution of the gas density profile (second panel in same figure). After sloshing sets in, both, metal density and metallicity, display discontinuities coincident with the ones in temperature and gas density. The contrast of metal density/metallicity depends clearly on the initial metal distribution: In case of the steep initial profile, the contrast across corresponding edges is higher. Inside the CFs, the metal profiles are approximately constant or even radially increasing. Even in the case of a steep initial metallicity gradient, sloshing can temporarily produce ridges of enhanced metallicity.

5.3 Comparison to observations

The two bottom panels of Fig. 9 display the evolution of the projected and azimutally averaged metallicity for the initially steep and flatter metal distribution. The CFs are easily recognisable as steep gradients in the profiles. Inside the

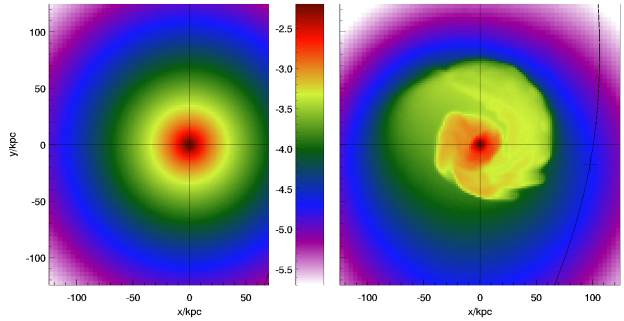

Figure 14. Synthetic projected metallicity map (in solar) for initial state (left) and 1.2 Gyr after subcluster pericentre passage (right), for the case of the flat (scale radius 120 kpc) initial metal distribution.

CFs, the projected metallicity forms plateaus, even in the steep case. The NW-SE asymmetry discussed in Sect. 4.5.3 is evident in the metallicity profiles, too.

Also in projection, the contrast of metallicity across the CFs depends on the initial distribution. In case of the steep initial profile, the contrast across the front is stronger, too strong compared to the observational data. Moreover, the overall projected metallicity profile is too steep compared to the observations. This already shows that the redistribution by sloshing alone is not sufficient to transform a steep metal peak originating from stellar mass loss of the central galaxy into the observed flattened one. Additional processes are required. It is also debatable whether the metal distribution about 1-2 Gyr ago should follow the current light profile of M87. If the metal peak in the Virgo centre was produced by stellar mass loss and SNIa, then the O/Fe profile should not be flat as observed (S10). More likely, the metal distribution originates from the assembly of M87 and has already undergone some redistribution.

For the initially pre-flattened case, we achieve a good agreement between observations and simulations (see Sect. 4). Therefore, we will concentrate on the initially flatter case for the further analysis.

Fig. 14 displays a metallicity map for the initially flatter metal distribution (lhs panel), and at 1.2 Gyr after the subcluster's pericentre passage. The orbital plane is seen face-on. The metallicity map displays a spiral coincident with the cool spiral in temperature maps and the brightness excess spiral in residual brightness maps. Interestingly, there is no metal-enhancement S of the southern CF, whereas the residual maps show a clear brightness excess there.

5.4 Broadening of the global metal distribution

5.4.1 General

Figure 15 demonstrates the effect of the sloshing on the global broadening of the metal distribution. We derive the cumulative metal mass and the spherically averaged metal density for different timesteps and compare them to the initial state. Apart from causing edges and plateaus in the directions of the CFs, the sloshing broadens the overall metal distribution, but only inside the outer CF radius, i.e., about 100 kpc. For the initially flatter case, within 1 Gyr after pericentre passage, the sloshing has depleted the central metal

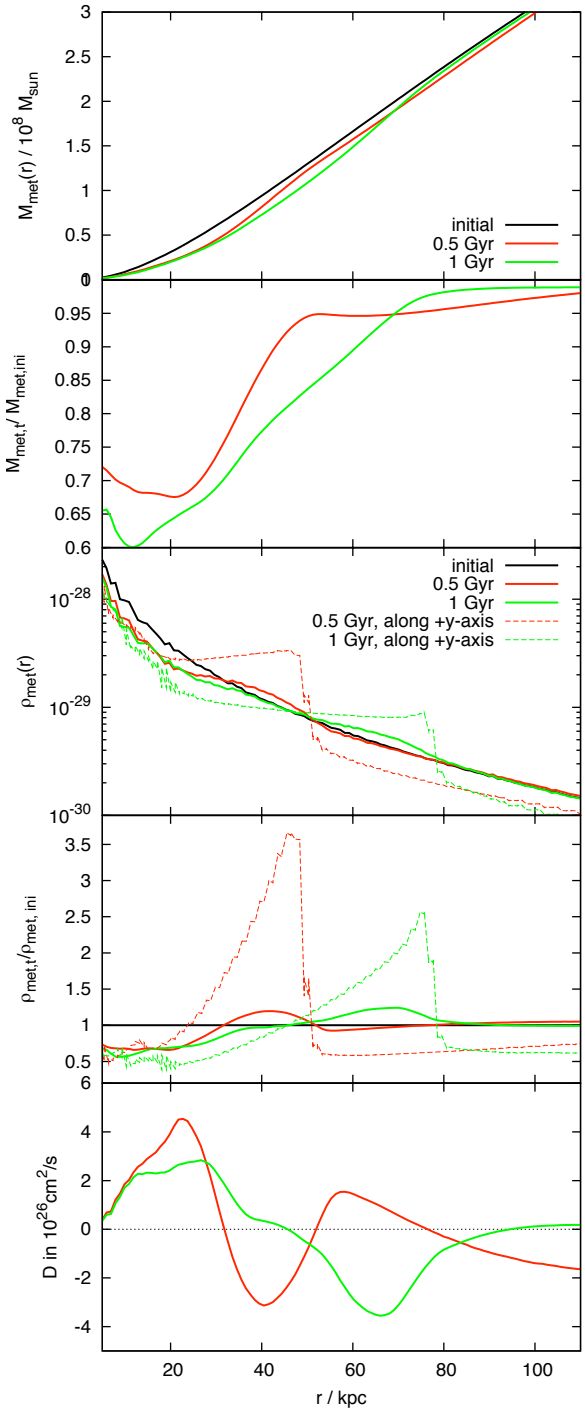

Figure 15. Effect of sloshing on the metal distribution. **Top:** cumulative metal mass for initial time and $t = 0.5, 1$ Gyr. **Second panel:** Relative change of cumulative metal mass: profiles from previous panel divided by initial distribution. **Third:** spherically averaged metal density (thick lines) for initial state and $t = 0.5, 1$ Gyr. The thin lines show the metal density along the $+y$-axis of the simulation grid. **Fourth:** Relative change of metal density profiles: profiles from previous panel divided by initial profile. **Fifth:** diffusion constant derived from profiles in third panel.

density by about 30%, and deposited these metals between 60 and 80 kpc, leading to an enhancement of the spherically averaged metal density by about 10 to 20% in this radial range. This is somewhat less than the 20 to 30% derived in S10, but there only the difference between the NW and the SE sector was compared, while we considered the global broadening.

Sloshing is, however, not a symmetric process, and the metal redistribution is much stronger if considered along a line directly towards a CF. We demonstrate this by overplotting the metal density along the $+y$-axis of the simulation grid in Fig. 15. Along this particular direction, the metal density is enhanced by a factor of 2 to 3 within the 20 kpc inside of the CF.

5.4.2 Diffusion description

Rebusco et al. (2005, 2006) used a diffusion description to model the broadening of the central metal distributions in clusters. They assumed that the metals originate mainly from the stellar mass loss of the central galaxy. Thus, their distribution should follow the light profile of the central galaxy. Turbulent gas motions have a diffusive effect on the metal distribution and broaden it to the observed shape. From this ansatz, Rebusco et al. (2006) derive an effective diffusion constant of the order of 10^{29} cm^2/s for several clusters. For the Virgo centre, they derive $0.8 \cdot 10^{29}$ cm^2/s. Graham et al. (2006) find a value of 10^{28} cm^2/s for the central region of the Centaurus cluster, but considerably smaller values outside 25 kpc. Roediger et al. (2007) have studied the metal mixing induced by AGN-inflated buoyantly rising bubbles. They found that such bubbles drag metal-rich gas from the centre to larger radii, effectively broadening the initial metal distribution. They derived effective diffusion coefficients that depended strongly on cluster radius, ranging from 10^{29} cm^2/s at about 10 kpc from the cluster centre to about 10^{26} cm^2/s at 50 kpc radius and 10^{22} cm^2/s at 100 kpc radius.

In order to quantify the effectiveness of sloshing in metal redistribution, we calculate the effective diffusion coefficients from our simulations in the same manner as in Roediger et al. (2007). We compare the spherically averaged density profiles at $t = 0.5, 1$ Gyr to the initial state. The result is shown by the thick lines in the bottom panel of Fig. 15. This plot immediately reveals that diffusion is not a good approximation for this redistribution process, because we derive negative, hence unphysical, diffusion constants in some parts. A close inspection reveals that the derived diffusion constant is negative inside the major CF, at those radii where sloshing deposits the metals it has removed from the centre. True diffusion would act differently: metals moved from the centre to some larger radius would not remain there but continue outwards until a flat distribution is achieved. In contrast, sloshing removes metals from the central parts and "piles them up" inside the CFs. Thus, the diffusion approximation must fail at these radii, which it does by leading to negative diffusion constants in these parts.

In the inner part, however, we derive a positive diffusion constant of the order of $2 \cdot 10^{26}$ cm^2/s between 10 and 30 kpc, which is less than what was derived for AGN activity. This may not be surprising, because AGN sit in very the centre of the cluster, thus their impact should be strongest there and decrease outwards. In contrast, the very central gas will be affected least by sloshing because it is held more tightly by the deep central gravitational potential. Thus, AGN activity and gas sloshing are complementary processes, the former being more effective in the very cluster centre, the latter at larger radii. In a realistic case, a combination of both could be very effective. Furthermore, the metal mixing by AGN induced buoyant bubbles is, on average, a continuous process, because a series of bubbles is inflated by intermittent AGN activity. In contrast, the sloshing studied here happens in the aftermath of a single event. Hence, the diffusion efficiency averaged over the whole event is rather low. If the effective diffusion constant is averaged over a much shorter time, e.g. 50 to 200 Myr, it is at least a factor of 10 higher. Also repeated minor merger events may enhance the efficiency of metal redistribution.

6 SUBCLUSTERS WITH GASEOUS ATMOSPHERES

Previous work (AM06) stresses that the subcluster needs to be gas free to produce CFs comparable to observations, because otherwise the ram pressure stripping of the gaseous atmosphere from the subcluster would leave observable traces not found in observations. Having constrained the mass and size of the subcluster responsible for the sloshing in Virgo, we want to answer the following questions:

- Can the subcluster responsible for the CFs in Virgo be really gas free?
- How would the signatures from the interaction with a gaseous subcluster differ from that with a gas-free subcluster?

6.1 Initial setup

We fill the fiducial subcluster M2a100 either with an extended or with a compact atmosphere. For the subcluster atmosphere we assume a constant temperature with a central drop described by

$$T(r) = T_0 \, \frac{1 + (r/r_{T0})^3}{D_T + (r/r_{T0})^3}, \tag{4}$$

where T_0 is the temperature of the subcluster gas at large radii, T_0/D_T the central temperature, and r_{T0} the scale radius of the cooler core. Demanding hydrostatic equilibrium, we can calculate the density and pressure profile for the subcluster gas. For the simplest case of a constant temperature, $T(r) = T_0$, these are

$$\frac{p(r)}{p_0} = \frac{\rho(r)}{\rho_0} = \exp\left(\frac{m_p G M_{\rm sub}}{k T_0} \left[\frac{1}{r + a_{\rm sub}} - \frac{1}{a_{\rm sub}}\right]\right), \tag{5}$$

where m_p is the mean particle mass in the subcluster atmosphere, and $M_{\rm sub}$ and $a_{\rm sub}$ are the mass and scale radius of the Hernquist potential describing the subcluster DM distribution.

We note that the slope in density and pressure is very sensitive to the temperature of the subcluster gas. The subcluster atmosphere truncates where its pressure drops below the ambient pressure of the main cluster's ICM. This truncation condition determines the size and total gas mass

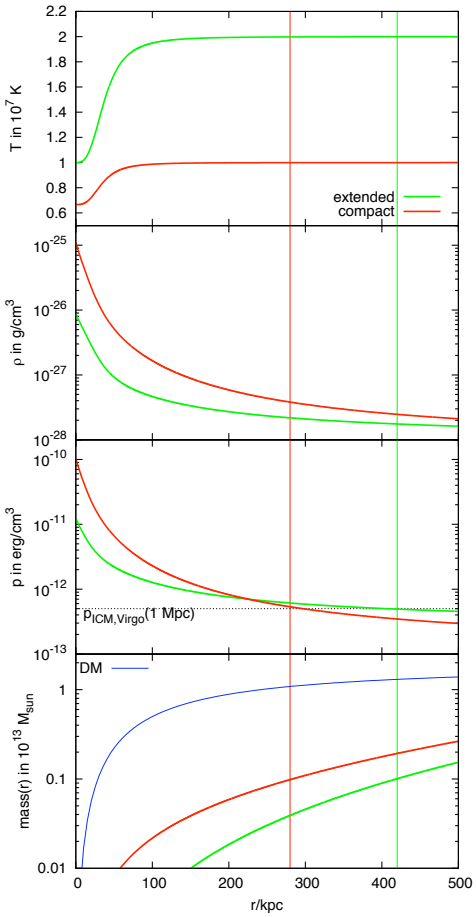

Figure 16. Gaseous atmospheres of subcluster. Extended and compact case. Panels show gas temperature, density, pressure, and cumulative mass. The green and red vertical lines mark approximately the extent of the atmosphere.

Table 6. Parameters for the gaseous subcluster atmospheres (see Sect. 6.1 for details).

	extended	compact
$T_0/10^7\,\mathrm{K}$	2	1
D_T	2	1.5
$r_{T0}/\,\mathrm{kpc}$	30	30
$\rho_0/\,\mathrm{g\,cm^{-3}}$	$8.8\cdot10^{-27}$	$1.1\cdot10^{-25}$

of the subcluster. We adopt an ambient ICM pressure of $5\cdot10^{-13}\,\mathrm{erg\,cm^{-3}}$ (typical for the Virgo cluster at 1 Mpc, according to gas profile fits in Fig. 2). Then we chose the temperature and density of the subcluster gas such that the subcluster gas pressure drops below the ambient ICM pressure at a radius such that, in both cases, the subcluster contains about the same amount of gas. For both cases, Fig. 16 shows density, temperature, pressure, and cumulative mass. Table 6 summarises the parameters for both atmospheres.

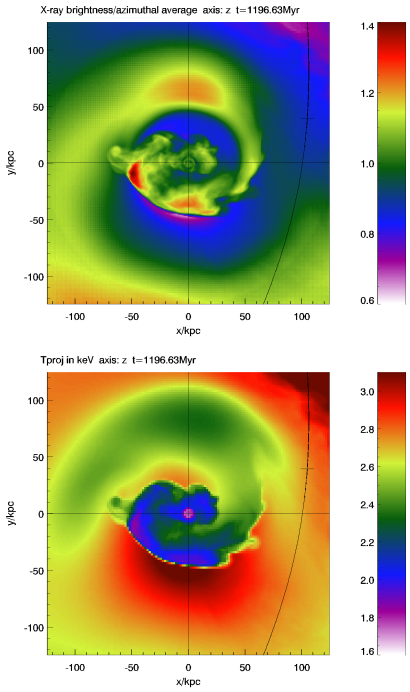

Figure 18. Fiducial orbit, fiducial subcluster M2a100, filled with extended gaseous atmosphere: The residual map and projected temperature map at $t = 1.2\,\mathrm{Gyr}$ are similar to the case without gas (Figs. 7, 8), although the temperature contrast between ambient gas and cool spiral is lower in the North.

6.2 Result

We send the gas-filled subclusters along the fiducial orbit with pericentre distance 100 kpc, starting with an initial separation of 1 Mpc, 1.7 Gyr prior to pericentre passage. The extended atmosphere is indeed ram-pressure-stripped prior to pericentre passage, and the resulting CF structures are similar to the corresponding case with gas-free subcluster (Fig. 18). The compact (and centrally denser) atmosphere is not stripped completely and causes a significant perturbation in the cluster centre (Fig. 17). This subcluster atmosphere may even survive if the subcluster moves along a fast orbit with $d_{\min} \geqslant 100\,\mathrm{kpc}$, because the peak ram pressure does not increase significantly (bottom panel of Fig. 3). We still get CF features similar to the gas-free case, but in a much more disturbed manner. This suggests that in the Virgo cluster, the subcluster was indeed gas-free before reaching the cluster centre.

7 SLOSHING TRIGGERED BY A GALAXY'S BOW SHOCK

Any process that offsets the ICM from a hydrostatic distribution on large scales (in a "bulk-like" manner) will cause subsequent sloshing and formation of CFs. An alternative to displacing the ICM by gravitational interaction with a subcluster is the passage of a shock, proposed by Churazov et al. (2003). These authors presented low resolution simulation of a shock passing a hydrostatic cluster. In their scenario, the

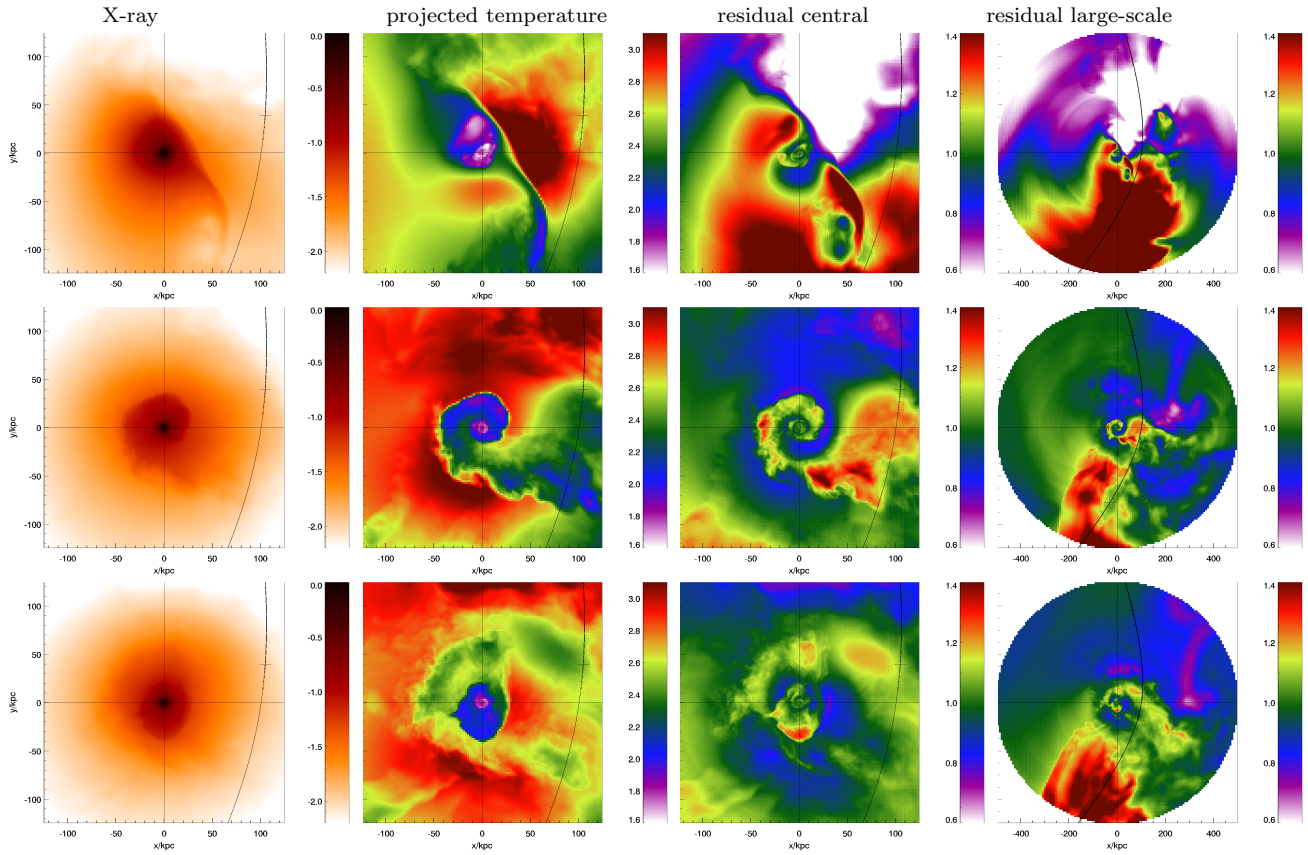

Figure 17. Fiducial orbit, fiducial subcluster M2a100dmin100, filled with a compact gaseous atmosphere: Here, the subcluster is not stripped completely and disturbs the cluster centre significantly. We show X-ray maps, projected temperature maps, and residual maps for the central region and a large field-of-view for three timesteps (one timestep per row: $t = 0.5, 1.2, 1.6$ Gyr).

shock originated from gas-rich subclusters falling into the Perseus cluster supersonically and driving a shock through the ICM. However, the shock was set up highly idealised as a plane shock.

We want to advance the idea of a shock as the cause of sloshing CFs and study the impact of a bow shock of a massive galaxy passing the Virgo core fast at a distance of 400 kpc (orbit "fast 400" in Fig 3). The large pericentre distance ensures that the tail of stripped gas will not appear in the close-up view of the Virgo cluster. The high velocity is needed to produce a sufficiently strong shock. In our simulation, the galaxy starts at a distance of 1.3 Mpc from the cluster centre (0.75 Gyr prior to pericentre passage) with a velocity of 1500 km s^{-1} approximately towards the cluster centre. The galaxy potential is described by a Hernquist halo with $2 \cdot 10^{12} M_{\odot}$ and scale radius 30 kpc. Initially, the galaxy contains a gaseous halo of $3 \cdot 10^6$ K and central density 10^{-24}g cm^{-3}. This gaseous halo will not be ram pressure stripped completely, so that this galaxy will be preceded by a bow shock. We note that the exact distribution of the gas in the galaxy does not matter as long as the galaxy can retain some gas and hence a bow shock. The galaxy may also be a spiral galaxy. The bow shock passes the Virgo core about 200 Myr after the closest approach of the galaxy, offsetting the gas by a few kpc, which leads to subsequent sloshing in a similar manner as described before.

Figure 19 demonstrates the resulting structure 1.3 Gyr after shock passage, i.e. 1.5 Gyr after pericentre passage of the galaxy. The morphology is similar to the gravitational interaction with the M1a100 subcluster passing at 100 kpc from the cluster centre. We find a cool-bright spiral, but the fronts are less sharp. At that time, no obvious trace of the interaction but the cool spiral and the spiral-shaped excess can be found. Making the galaxy pass closer to the cluster centre would increase the contrast and probably cause the fronts to be sharp. If however the galaxy passes too close to the core, its stripped tail will be visible in the central region, which is not observed in Virgo. It is important to note that the figures for the galaxy passage are rotated by 180^o to have the spiral in the same orientation as the observation and previous simulations. This means that in order to reproduce the observed orientation of the excess spiral in Virgo, the galaxy must have passed the cluster core in the east going approximately from south to north, which is the opposite side and direction compared to the passing gas-free subclusters. The responsible galaxy would now be located about 2.2 Mpc north of Virgo. The reason for this inversion is that the initial displacement is not a pull towards the subcluster/galaxy but a push from the bow shock.

We conclude that structures similar to the ones associated with sloshing CFs can be produced by strong bow shocks of galaxies, but the fronts are not as sharp as ob-

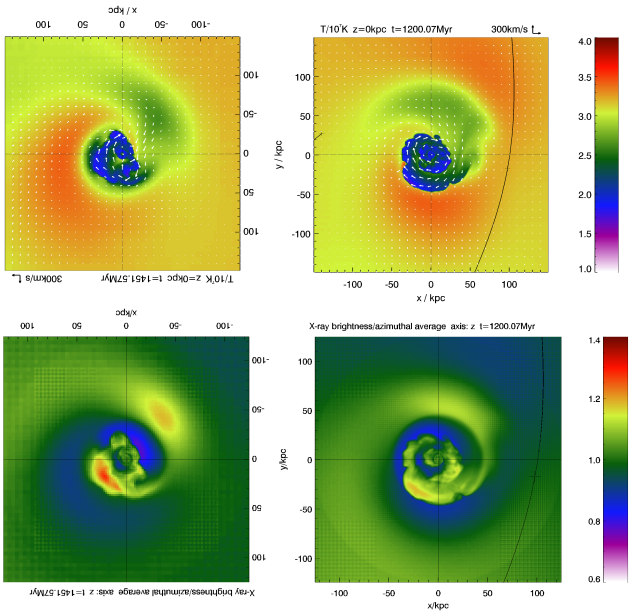

Figure 19. Comparison of colour-coded temperature slices (top row) and residual maps (bottom row) for two different scenarios: a bow shock of a fast galaxy passing at 400 kpc from cluster centre triggered sloshing (lhs), and the usual gravitationally triggered sloshing (rhs). However, the sloshing was triggered by the less massive subcluster M1a100dmin100. Note that the figures for the galaxy passage are rotated by 180 degree. See also Sect. 7.

served. Fine-tuning between a closer pericentre distance with just avoiding the stripped tail appearing in the central region, or a more refined galaxy model may lead to sharper CFs. Moreover, the triggering of sloshing by the passage of a bow shock is also attractive when regarding merger rates: passages of a $2 \cdot 10^{12} M_{\odot}$ galaxy may be more frequent than passages of $> 10^{13} M_{\odot}$ subclusters.

In summary, our test simulation of the bow-shock triggered sloshing can reproduce the cold front structures in Virgo qualitatively, but quantitatively leave a too weak signature.

8 DISCUSSION

8.1 Reliability of our model

The strongest limitation of our model is the restriction to rigid potentials. As discussed in Sect. 2, in our simulation the impact of a subcluster of a given mass will be somewhat overestimated. Thus, the derived required mass for the subcluster is strictly speaking a lower limit. However, much more massive subclusters can be excluded, because the interaction would be no more a minor but a major merger, whose characteristic traces are not seen in Virgo.

Despite the simplification to rigid potentials, our simulations reproduce the orientation of the spiral CF structure as seen in hydro+Nbody simulations (AM06, ZuHone et al. 2010). Also the large-scale brightness asymmetry predicted by our simulations should also be found in hydro+Nbody simulations. The strength of this asymmetry could be weaker in reality because the outgoing subcluster would have suffered tidal truncation. Thus it would contain less mass and have less impact on the outer cluster parts. However, a brightness excess feature at several 100 kpc from the cluster centre like the predicted one is found in some clusters (Sect. 4.6), indicating that the large-scale signature is real. A quantitative study requires hydro+Nbody simulations. So far, no full hydro+Nbody simulations with our spatial resolution have been performed, but are planned for forthcoming work.

In our idealised mergers, the choice of the initialisation time is somewhat arbitrary. In Appendix B we demonstrate that our results are not very sensitive to this choice and consistently predict the radius of the CFs within $\pm 10\%$.

The results presented and discussed in this paper are also resolution independent, as shown in Appendix A.

8.2 Stability of CFs

CFs are expected to be associated with shear motions, which should lead to the formation of Kelvin-Helmholtz instabilities (KHIs). We indeed observe this instability in our simulations, although it is not omnipresent. Clear shear flows strong enough to cause KHIs are established only ~ 700 Myr after the subcluster passed the main core, hence, the instability occurs only in the later stages of evolution. Subclusters with shallow potentials induce a weaker velocity field in the ICM without clear shearing layers, and consequently no significant KHI occurs. However, the subclusters with potentials deep enough to produce structures comparable to the observed ones, also cause KHIs.

KHIs are believed to destroy CFs. As this is a dynamic process and takes some time, it would be interesting if we could learn something from the observed azimuthal extent of the CFs, e.g. if we could constrain the scale length of KH modes at work and consequently constrain transport coefficients of the ICM. This task is difficult for our simulations because they are idealised. However, we find that the CFs are never destroyed completely, but are reformed continuously. The task might even be intrinsically difficult: in Appendix A we show that in projection the CFs appear less disturbed in the case of the highest resolution, although here the KHI is clearly present. In projection, the fine KH structures average out. Thus, CFs may appear sharp in projection although the KHI is taking place. Hence, the fact that no clear KH rolls are detected in observations does not imply that the KHI does not take place.

We note that the KHI is apparent in images taken perpendicular to the orbital plane only, but is nearly absent if the images are taken along a LOS parallel to the orbital plane.

8.3 Impact of sloshing on the radio lobes

The central active galactic nucleus (AGN) of the Virgo cluster has induced a rich structure inside the inner ~ 30 kpc of the ICM, including radio lobes and cavities. The radio lobes show a peculiar morphology: while the eastern arm is extends straight out to about 30 kpc, the western arm is bent sharply southwards at about 20 kpc from the cluster centre. S10 discussed the possibility that the western arm is bent due to the same sloshing motions that cause the CFs. In Fig. 20 we compare the central velocity field of our simulations and the observed radio lobes (middle figure from

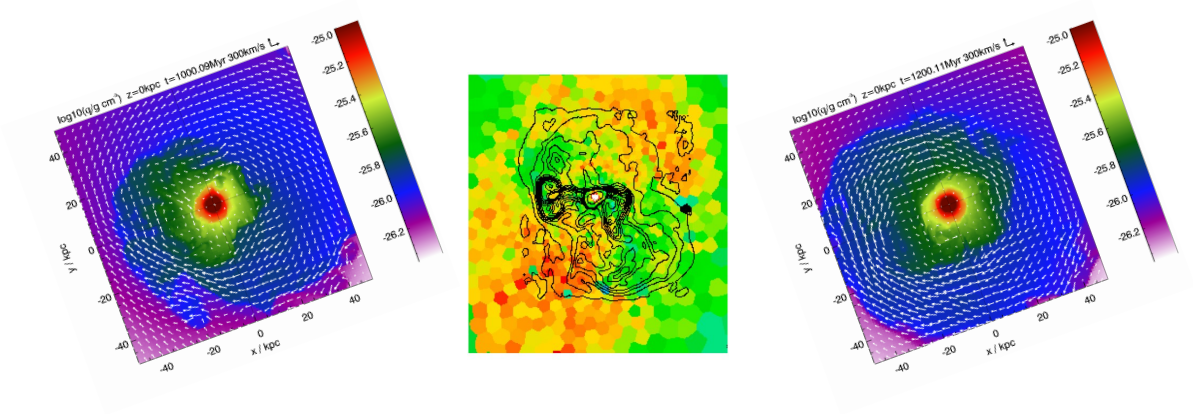

Figure 20. Zoom-in of velocity field and density field in simulation (left, right, for $t = 1$ and 1.2 Gyr of our fiducial run), observed pressure deviations and radio lobes (middle, Simionescu et al. 2007).

S10). In the central 15-20 kpc, the velocity field is weak and unlikely to modify the AGN outflow. Outside 20 kpc west from the core, the velocity field is characterised by a $\sim 250\,\mathrm{km\,s^{-1}}$ southward flow. This direction and position matches the bending of the western radio lobe. East of the cluster core, a northward flow sets in at about ~ 30 kpc from the centre. Hence, the asymmetry of the sloshing velocity field could explain the bending.

9 SUMMARY

We perform a set of hydrodynamical simulations of minor-merger induced gas sloshing and the subsequent formation of sloshing cold fronts. For the first time, these simulations aim at reproducing the characteristics of the cold fronts and associated structures observed in a specific cluster not only qualitatively, but also quantitatively. In this paper, our target is the Virgo cluster.

By comparing synthetic and real observations in great detail, we show that the sloshing scenario can reproduce the known characteristics: a pair of CFs, their radius, the contrast in X-ray brightness, projected temperature, and metallicity across the fronts, and a spiral-shaped brightness excess.

Furthermore, we identify additional, so far unreported, features typical for sloshing cold fronts. (i) X-ray brightness excess regions alternate with brightness deficit regions. Exactly spatially consistent structures are found temperature and metallicity maps, where brightness excess corresponds to cool, metallicity enhanced regions and vice versa. This alternating behaviour is also evident when overplotting profiles across the opposite CFs. (ii) Inside each cold front, the temperature profile is constant or radially decreasing, and is accompanied by a plateau in metallicity. (iii) On the outside, the CFs are bordered by a warm rim. (iv) On a larger scale of a few 100 kpc, there is a typical large-scale brightness excess towards the direction of the responsible subcluster, which will be helpful in identifying the responsible subcluster. We can trace these new features not only in Virgo, but also in other clusters exhibiting sloshing CFs.

Our constraints on the subcluster responsible for the CFs in Virgo are the following: From the size of the observed CF structure, we constrain the age of the CF structure in Virgo to 1-1.2 Gyr. The presence of the spiral-shaped brightness excess suggests that our line-of-sight to be nearly perpendicular to the orbital plane. The contrasts of X-ray brightness and temperature across the fronts, exclude subcluster masses below $10^{13} M_\odot$ and above $\sim 4 \cdot 10^{13} M_\odot$. Near-head-on encounters are excluded on the basis of an intact cool core in Virgo. The subcluster mass and pericentre distance of the orbit are degenerate to some degree, but constrained between the cornerstones ($2 \cdot 10^{13} M_\odot$, 100 kpc pericentre distance), and ($4 \cdot 10^{13} M_\odot$, 400 kpc pericentre distance). The responsible subcluster must currently be located south of the Virgo centre. Its orbital velocity is no crucial parameter, thus its current distance can be constrained between 1 and 2 Mpc only. We suggest the galaxy group around NGC 4365, currently about 5^o (1.6 Mpc) south of the Virgo centre (about 500 kpc west-south-west of M49) as the most likely culprit.

Additionally, we quantify the metal redistribution by sloshing in Virgo. We demonstrate that sloshing alone cannot transform a peaked metal distribution proportional to the stellar mass density in M87 to the observed flattened one. We also demonstrate that diffusion is inept to describe this particular redistribution process.

To complete our analysis, firstly we show that the responsible subcluster can indeed be completely ram pressure stripped before pericentre passage as required by the standard scenario, and thus leaves no traces but the observed ones in Virgo. However, a compact gaseous atmosphere might survive beyond the pericentre passage and leave additional features in the Virgo ICM. Secondly, we demonstrate that the bow shock of a fast galaxy passing the Virgo cluster at ~ 400 kpc distance also causes sloshing and leads to very similar, though somewhat weaker CF structures. The responsible galaxy would be located nearly 2.2 Mpc north of the Virgo centre.

ACKNOWLEDGMENTS

We acknowledge the support of the Priority Programme "Witnesses of Cosmic History" of the DFG (German Research Foundation) and the supercomputing grants NIC 3229 and 3711 at the John-Neumann Institut at the Forschungszentrum Jülich. AS acknowledges the support

provided by NASA through Einstein Postdoctoral Fellowship grant number PF9-00070 awarded by the Chandra X-ray Center, which is operated by the Smithsonian Astrophysical Observatory for NASA under contract NAS8-03060. We thank John ZuHone and Ryan Johnson for helpful discussions. The results presented were produced using the FLASH code, a product of the DOE ASC/Alliances-funded Center for Astrophysical Thermonuclear Flashes at the University of Chicago.

REFERENCES

Ascasibar Y., Markevitch M., 2006, ApJ, 650, 102
Biller B. A., Jones C., Forman W. R., Kraft R., Ensslin T., 2004, ApJ, 613, 238
Binggeli B., Popescu C. C., Tammann G. A., 1993, A&ASS, 98, 275
Binggeli B., Sandage A., Tammann G. A., 1985, AJ, 90, 1681
Binggeli B., Tammann G. A., Sandage A., 1987, AJ, 94, 251
Birnboim Y., Keshet U., Hernquist L., 2010, eprint arXiv:1006.1892
Bourdin H., Mazzotta P., 2008, A&A, 479, 307
Cavagnolo K. W., Donahue M., Voit G. M., Sun M., 2009, ApJSS, 182, 12
Churazov E., Forman W. R., Jones C., Bohringer H., 2003, ApJ, 590, 225
Churazov E., Forman W. R., Vikhlinin a., Tremaine S., Gerhard O., Jones C., 2008, MNRAS, 388, 1062
Ciotti, L. Bertin G., 1999, A&A
Clarke T. E., Blanton E. L., Sarazin C. L., 2004, ApJ, 616, 178
Dubey A., Antypas K., Ganapathy M. K., Reid L. B., Riley K., Sheeler D., Siegel A., Weide K., 2009, Parallel Computing, 35, 512
Dupke R., White III R. E., Bregman J. N., 2007, ApJ, 671, 181
Fabian A. C., Sanders J. S., Ettori S., Taylor G. B., Allen S. W., Crawford C. S., Iwasawa K., Johnstone R. M., 2001, MNRAS, 321, L33
Fabian A. C., Sanders J. S., Taylor G. B., Allen S. W., 2005, MNRAS, 360, L20
Ghizzardi S., Rossetti M., Molendi S., 2010, A&A, 516, A32
Graham J., Fabian A. C., Sanders J. S., Morris R. G., 2006, MNRAS, 368, 1369
Heinz S., Churazov E., Forman W. R., Jones C., Briel U. G., 2003, MNRAS, 346, 13
Hernquist L., 1990, ApJ, 356, 359
Irwin J. A., Sarazin C. L., 1996, ApJ, 471, 683
Keshet U., Markevitch M., Birnboim Y., Loeb A., 2009, eprint arXiv:0912.3526
Kormendy J., Fisher D. B., Cornell M. E., Bender R., 2009, ApJSS, 182, 216
Kraft R., Forman W. R., Jones C., Nulsen P. E. J., Hardcastle M. J., Evans D. A., Raychaudhury S., Sivakoff G., Sarazin C., Murray S. S., 2009, in Chandra's First Decade of Discovery An X-ray Study of the Nearby Massive Early-Type Galaxy NGC 4472
Lufkin E. A., Balbus S. A., Hawley J. F., 1995, ApJ, 446, 529
Markevitch M., Gonzalez A. H., David L., Vikhlinin A., Murray S., Forman W. R., Jones C., Tucker W., 2002, ApJ, 567, L27
Markevitch M., Ponman T. J., Nulsen P. E. J., Bautz M. W., Burke D. J., David L. P., Davis D., Donnelly R. H., Forman W. R., Jones C., Kaastra J., Kellogg E., Kim D., Kolodziejczak J., Mazzotta P., Pagliaro A., Patel S., Van Speybroeck L., Vikhlinin A., Vrtilek J., Wise M., Zhao P., 2000, ApJ, 541, 542
Markevitch M., Vikhlinin A., 2007, Physics Reports, 443, 1
Markevitch M., Vikhlinin A., Mazzotta P., 2001, ApJ, 562, L153
Matsushita K., Belsole E., Finoguenov A., Böhringer H., 2002, A&A, 386, 77
Mazzotta P., Edge A. C., Markevitch M., 2003, ApJ, 596, 190
Mazzotta P., Giacintucci S., 2008, ApJ, 675, L9
Mazzotta P., Markevitch M., Vikhlinin A., Forman W. R., David L. P., VanSpeybroeck L., 2001, ApJ, 555, 205
Mazzotta P., Rasia E., Moscardini L., Tormen G., 2004, MNRAS, 354, 10
Million E. T., Allen S. W., 2009, MNRAS, 399, 1307
Million E. T., Allen S. W., Werner N., Taylor G. B., 2009, eprint arXiv:0910.0025
Owers M. S., 2008, Phd, University of New South Wales
Owers M. S., Nulsen P. E. J., Couch W. J., Markevitch M., 2009, ApJ, 704, 1349
Owers M. S., Nulsen P. E. J., Couch W. J., Markevitch M., Poole G. B., 2009, ApJ, 692, 702
Prugniel, P. Simien F., 1997, A&A
Randall S. W., Jones C., Markevitch M., Blanton E. L., Nulsen P. E. J., Forman W. R., 2009, ApJ, 700, 1404
Rebusco P., Churazov E., Böhringer H., Forman W. R., 2005, MNRAS, 359, 1041
Rebusco P., Churazov E., Böhringer H., Forman W. R., 2006, MNRAS, 372, 1840
Roediger E., Brüggen M., Rebusco P., Böhringer H., Churazov E., 2007, MNRAS, 375, 15
Sanders J. S., Fabian A. C., 2006, MNRAS, 371, 1483
Sanders J. S., Fabian A. C., Dunn R. J. H., 2005, MNRAS, 360, 133
Sanders J. S., Fabian A. C., Taylor G. B., 2005, MNRAS, 356, 1022
Sanders J. S., Fabian A. C., Taylor G. B., 2009a, MNRAS, 396, 1449
Sanders J. S., Fabian A. C., Taylor G. B., 2009b, MNRAS, 393, 71
Sersic J. L., 1963, Boletin de la Asociacion Argentina de Astronomia, 6, 41
Simionescu A., Böhringer H., Brüggen M., Finoguenov A., 2007, A&A, 465, 749
Simionescu A., Werner N., Forman W. R., Miller E. D., Takei Y., Böhringer H., Churazov E., Nulsen P. E. J., 2010, MNRAS, 405, 91
Tanaka T., Kunieda H., Hudaverdi M., Furuzawa A., Tawara Y., 2006, PASJ, 58, 703
Tittley E. R., Henriksen M., 2005, ApJ, 618, 227
van de Ven G., Mandelbaum R., Keeton C. R., 2009, MNRAS, 398, 607

van den Bosch R. C. E., van De Ven G., Verolme E. K., Cappellari M., de Zeeuw P. T., 2008, MNRAS, 385, 647
Vikhlinin A., Markevitch M., Murray S. S., 2001, ApJ, 551, 160
ZuHone J. A., Markevitch M., Johnson R. E., 2010, eprint arXiv:0912.0237

APPENDIX A: RESOLUTION TEST

The formation mechanism of CFs is accompanied by shear motions which are prone to KH instability. In this instability, the small-scale modes grow fastest, hence, in simulations, their evolution can be resolution-dependent. In our simulations, KHIs play a minor role in cases with shallow subcluster potentials. In the fiducial run and cases with deeper subcluster potentials, KHIs appear at $t \gtrsim 700$ Myr, because here for the first time a larger region with a clear shear flow is established. KH rolls are also present in these simulations at the stage when the CF radius has reached the observed value (approx. $t = 1$ Gyr).

We test our fiducial run in 3 resolutions. Figure A1 displays temperature slices in the orbital plane for our standard resolution, a factor of 2 less and a factor of 2 better. In the standard resolution, the inner 60 kpc are resolved by 1 kpc, the inner 120 kpc are resolved by 2 kpc. The overall structure, regarding size and contrast across CFs, is independent of resolution. The fronts are discontinuities within the resolution for all cases. Even with highest resolution, KH instabilities appear only after 700 after core passage. At no time the CFs are completely disrupted. With better resolution, KHI takes place at smaller scales. The sloshing motion continuously reforms the CFs.

In projection, the KHIs are less pronounced (see X-ray images, residual images, projected temperature maps in Fig. A2). In the run with the highest resolution, the KH rolls are even more difficult to detect than in the standard resolution run, because in projection, the fine structure averages out. Thus, CFs may appear sharp in projection although KHI is taking place. Hence, conclusion that existence of CFs without obvious KH rolls proves their absence has to be made cautiously. The large-scale signature reported in Sect. 4.6 does not depend on resolution. Neither do the azimuthally averaged profiles of X-ray brightness, projected temperature and metallicity (Fig. A3).

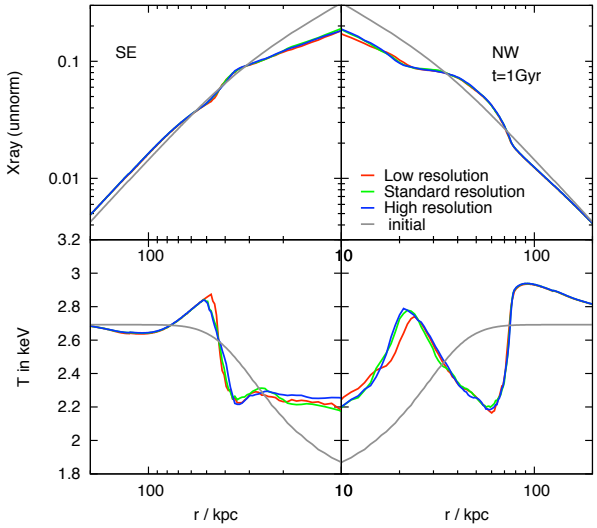

Figure A3. Projected, azimuthally averaged profiles of X-ray brightness and projected temperature (similar to Fig. 9), at $t = 1$ Gyr, for three resolutions differing by a factor of 2 (colour-coded, see legend).

APPENDIX B: INFLUENCE OF INITIAL SEPARATION

We simulate idealised mergers in the rest frame of the main cluster. In order to start a simulation for a given orbit, we have to place the subcluster at some point along this orbit and initialise it with the appropriate velocity. This initial position corresponds to the initialisation time, $t_{\rm ini}$, prior to pericentre passage (which takes place at $t = 0$). The choice of this $t_{\rm ini}$ is somewhat arbitrary. Choosing an early $t_{\rm ini}$, i.e. a large initial separation between subcluster and main cluster, ensures capturing the early influence of subcluster. However, we are interested in the evolution of the ICM in the main cluster centre only. As long as the subcluster is far from the main cluster centre, its influence is very small. A late $t_{\rm ini}$, i.e. a smaller initial separation, may be sufficient, and it reduces computational costs. Moreover, including the early influence of the subcluster in our rigid potential simulations may even cause unrealistic effects: While the subcluster is approaching the main cluster core, both, the core gas and the DM peak should move slowly towards the subcluster, but in the rigid potential approximation, only the core gas can move. Thus, already the mere presence of the subcluster will cause a slight offset of the ICM from its initially hydrostatic distribution. Like any other offset, this will lead to gas sloshing, though at a very low amplitude. The state of this premature sloshing depends on $t_{\rm ini}$, and may have a slight influence on the major sloshing triggered by the pericentre passage of the subcluster. To assess this issue, we test in detail the importance of the initial separation by comparing simulations of our fiducial run that differ only in initial separation: $t_{\rm ini} = -1.7$ (maximal separation), -1.5, -1, -0.8, -0.5 Gyr.

In Fig. B1, we display temperature slices and velocity fields in the orbital plane of three of these test runs. The first row shows slight differences in the temperature structure and velocity field of the central ICM at 0.1 Gyr prior to pericentre passage. These differences arise because the premature minor sloshing explained above has had different amounts of time to evolve. Between pericentre passage ($t = 0$) and $t = 0.5$ Gyr, the sloshing triggered by the pericentre passage of the subcluster clearly dominates and proceeds in a very similar manner. The temperature structure and velocity fields are almost independent of $t_{\rm ini}$, except that for $t_{\rm ini}$ earlier than -1500 Myr the northern CF (along (0,1)-direction) is surrounded by a cooler region. This difference leads to a differing behaviour for the northern CF. For runs with $t_{\rm ini} \leqslant -1500$ Myr, at about $t = 700$ Myr, the bulk of the cool gas in the northern cool arm falls back towards the cluster centre and leaves behind an only mildly cool spiral

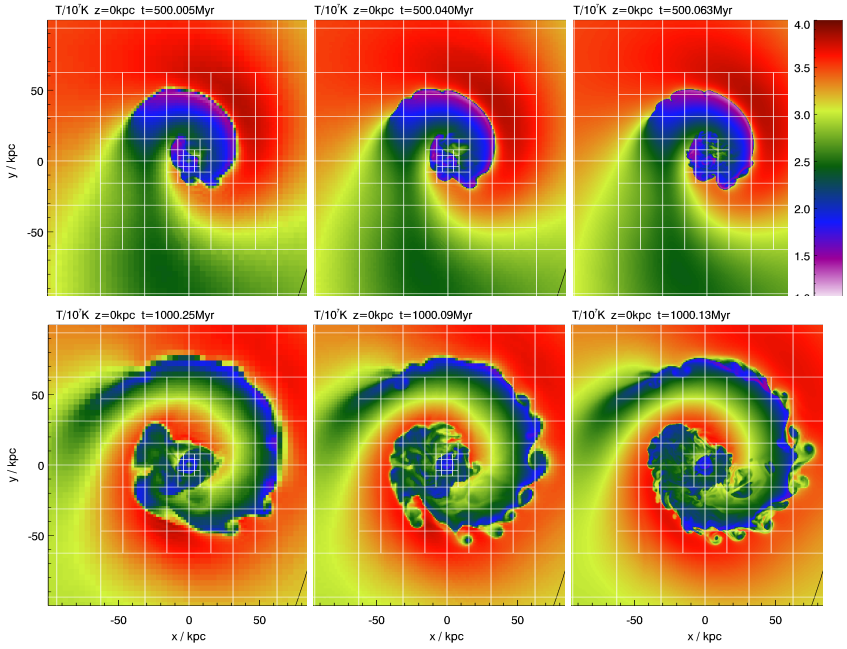

Figure A1. Impact of resolution on our simulations in fiducial run: Colour-coded temperature slices in the orbital plane. White boxes demonstrate resolution, one box corresponds to one "block" of grid cells. Three different resolutions are shown: Left: low resolution (1 block=8^3 cells). Middle: standard resolution (1 block=16^3 cells). Right: High resolution (1 block=32^3 cells). Two timesteps are shown: 0.5 Gyr (top row) and 1 Gyr (bottom row).

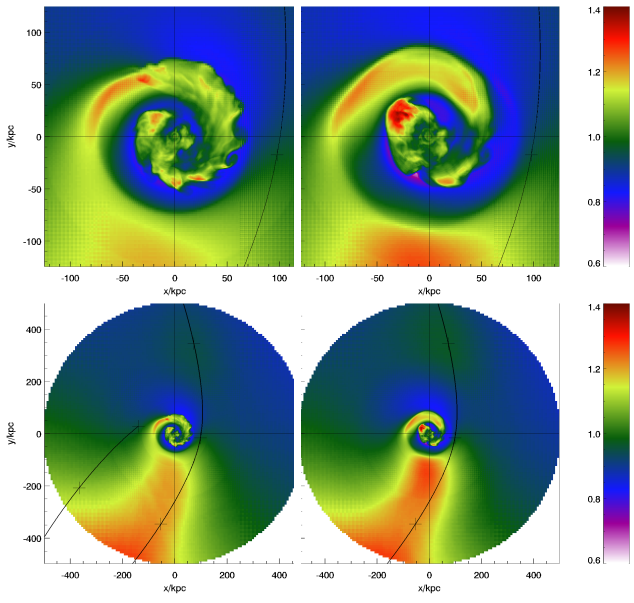

Figure B2. Residual maps, cluster centre (top row), and large-scale view (bottom row). Lhs column is for run with $t_{\rm ini} = -0.5\,$Gyr, rhs is for run with $t_{\rm ini} = -1\,$Gyr.

arm in the North. For $t_{\rm ini} = -1000\,$Myr and earlier, however, the northern CF evolves consistently, with the weak trend that for earlier $t_{\rm ini}$, the extent of the northern CF is slightly larger. We note that also the mildly cold northern spiral arm in the runs with very early $t_{\rm ini}$ is in a position consistent with the position of the cold northern arm in the other runs. In contrast, the southern part of the cool spiral evolves very similarly for all $t_{\rm ini}$. The different behaviour of the northern arm for runs with an early $t_{\rm ini}$ is an artefact of our rigid potentials. The earlier $t_{\rm ini}$, the more time there is to build up an unrealistic flow field. Hence, we disregard $t_{\rm ini}$ earlier than $-1\,$Gyr.

We compared temperature profiles in the xy-plane, averaged azimuthally over $\pm 20^o$ towards several directions. Taking into account only runs with $t_{\rm ini} = -1\,$Gyr or later, we inferred that our simulations consistently predict the position of the northern and southern CFs within $\pm 10\%$ or $\pm 5\,$kpc (for early times where the CF radius is small). Using the radius of the outer (northern) CF as an age estimator, this uncertainty in radius translates into an uncertainty of $\pm 200\,$Myr in age.

The spiral-shaped or staggered shell-shaped morphology of the CFs in the residual maps is independent of $t_{\rm ini}$, so is our prediction of the large-scale excess associated with the outgoing orbit (see Fig. B2).

We have tested the influence of $t_{\rm ini}$ for several different subclusters. In Fig. B3, we compare projected, azimuthally averaged profiles of X-ray brightness and temperature at $t = 1\,$Gyr for two sets of simulations. The line colour codes the subcluster and orbit parameters. Solid lines are for runs with $t_{\rm ini} = -0.5\,$Gyr, dashed lines for runs with $t_{\rm ini} = -1\,$Gyr. The profiles depend only slightly on $t_{\rm ini}$. Again, the CF radius predicted by runs with different $t_{\rm ini}$ agrees to about $\pm 10\%$. Only the case with a very massive, compact subcluster passing near the cluster core (M4a100dmin100) shows significant differences, but still qualitative agreement. Here, the subcluster mass is quite high (similar to the mass inside

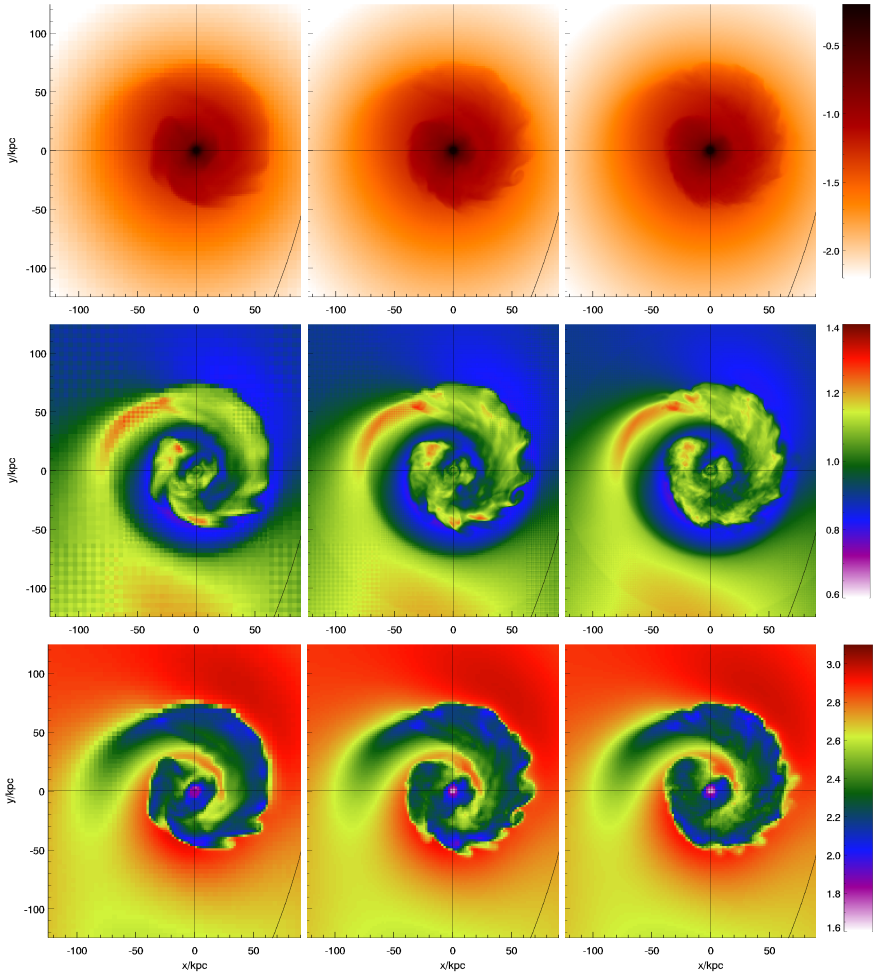

Figure A2. Projected Xray brightness (top row), residual maps (second row), projected temperature maps (bottom row). Lhs column is low resolution run, middle column standard resolution, rhs column high resolution run (compare Fig A1).

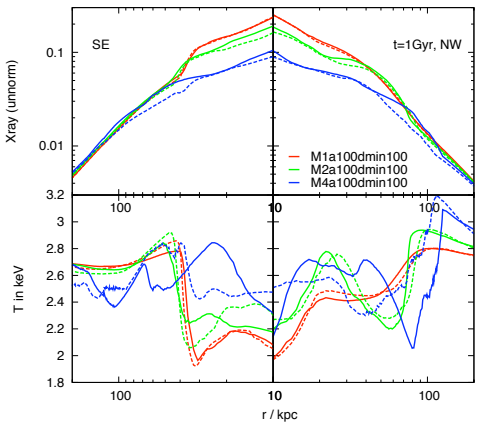

Figure B3. Azimutally averaged radial profiles of projected Xray brightness (unnormalised) and projected temperature (similar to Fig. 9). Lhs column is for SE cold front, rhs column is for NW cold front. Colour codes subcluster characteristics (mass, scale radius, orbit, see legend). Solid lines are for $t_{\rm ini} = -0.5$ Gyr, dashed for $t_{\rm ini} = -1$ Gyr.

the central 300 kpc of the Virgo cluster), and our approximation to rigid potentials reaches its limit.

We note that all qualitative results and conclusions are independent of $t_{\rm ini}$.

In order to capture the early evolution with as little contamination by the discussed artefact, we chose as the most representative setting an initial separation of $t_{\rm ini} = -0.5$ Gyr for all simulations with gas-free subclusters.

This paper has been typeset from a TEX/ LATEX file prepared by the author.

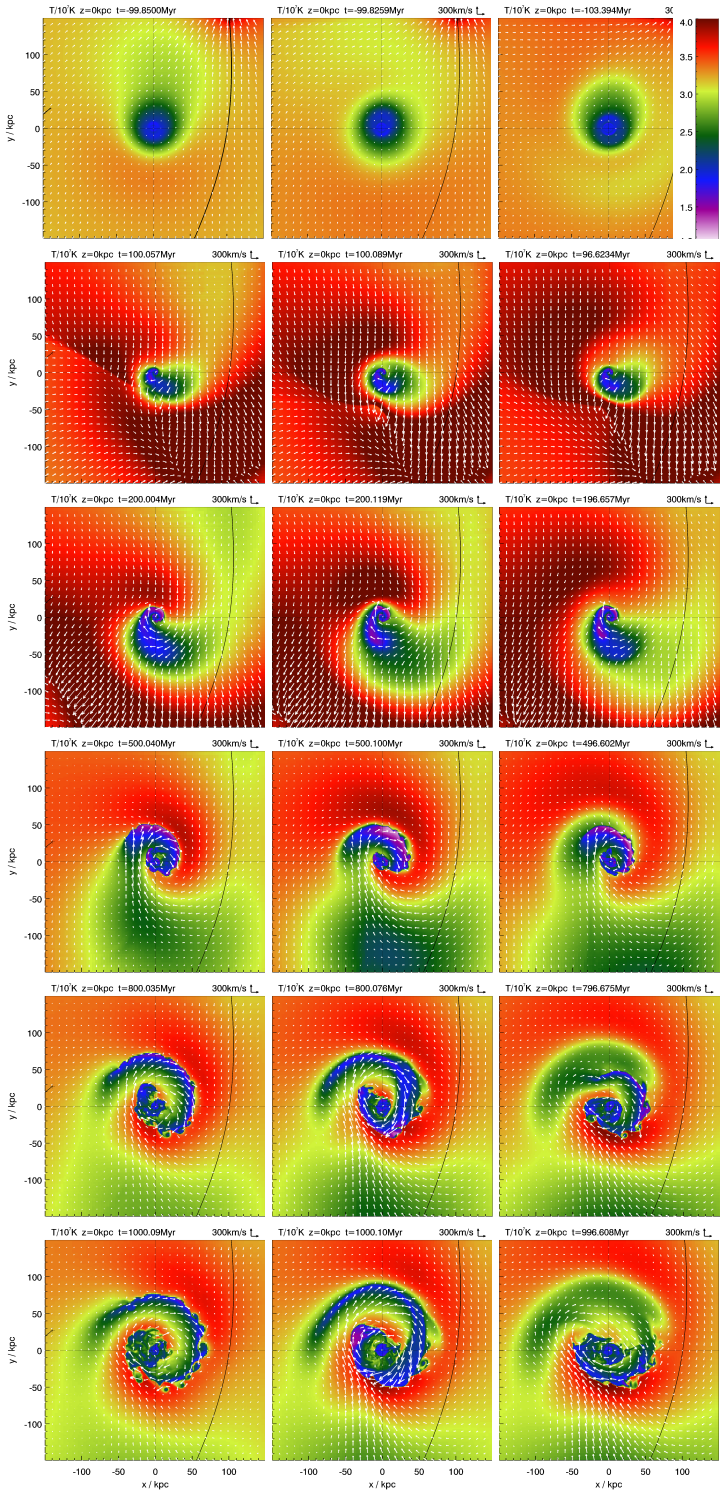

Figure B1. Temperature slices at different timesteps (rows). Each column is for one simulation run. Runs are for the same physical setup M2a100dmin100, but differ in initialisation time, $t_{\rm ini}$. Left: $t_{\rm ini} = -0.5\,{\rm Gyr}$. Middle: $t_{\rm ini} = -1\,{\rm Gyr}$. Right: $t_{\rm ini} = -1.78\,{\rm Gyr}$. Pericentre passage is at $t = 0$.